Uenzelmann-Neben, G., Bohaty, S.M., Childress, L.B., and the Expedition 392 Scientists
Proceedings of the International Ocean Discovery Program Volume 392
publications.iodp.org

Site U1582[1]

Keywords
International Ocean Discovery Program, IODP, *JOIDES Resolution*, Expedition 392, Agulhas Plateau Cretaceous Climate, Climate and Ocean change, Earth Connections, Site U1582, Cretaceous/Paleogene boundary, K/Pg boundary, Paleocene/Eocene Thermal Maximum, PETM, large igneous province, LIP, zeolite authigenesis, igneous sill intrusion, Campanian, Oligocene pelagic carbonates, paleoceanography, African–Southern Ocean gateway

Core descriptions

Supplementary material

References (RIS)

MS 392-106
Published 19 August 2023

Funded by NSF OCE1326927

S.M. Bohaty, G. Uenzelmann-Neben, L.B. Childress, O.A. Archontikis, S.J. Batenburg, P.K. Bijl, A.M. Burkett, H.C. Cawthra, P. Chanda, J.J. Coenen, E. Dallanave, P.C. Davidson, K.E. Doiron, J. Geldmacher, D. Gürer, S.J. Haynes, J.O. Herrle, Y. Ichiyama, D. Jana, M.M. Jones, C. Kato, D.K. Kulhanek, J. Li, J. Liu, J. McManus, A.N. Minakov, D.E. Penman, C.J. Sprain, A.C. Tessin, T. Wagner, and T. Westerhold[2]

[1] Bohaty, S.M., Uenzelmann-Neben, G., Childress, L.B., Archontikis, O.A., Batenburg, S.J., Bijl, P.K., Burkett, A.M., Cawthra, H.C., Chanda, P., Coenen, J.J., Dallanave, E., Davidson, P.C., Doiron, K.E., Geldmacher, J., Gürer, D., Haynes, S.J., Herrle, J.O., Ichiyama, Y., Jana, D., Jones, M.M., Kato, C., Kulhanek, D.K., Li, J., Liu, J., McManus, J., Minakov, A.N., Penman, D.E., Sprain, C.J., Tessin, A.C., Wagner, T., and Westerhold, T., 2023. Site U1582. In Uenzelmann-Neben, G., Bohaty, S.M., Childress, L.B., and the Expedition 392 Scientists, Agulhas Plateau Cretaceous Climate. Proceedings of the International Ocean Discovery Program, 392: College Station, TX (International Ocean Discovery Program). https://doi.org/10.14379/iodp.proc.392.106.2023
[2] **Expedition 392 Scientists' affiliations.**

1. Background and objectives

The northern Agulhas Plateau is characterized by a rough topography and a number of basement highs separated by depressions with only a thin sedimentary cover. In between the interpreted basement highs, thicker sediment packages filling depressions or sediment drifts are observed. This distribution of sedimentary sequences attests to the strong erosional/nondepositional influence of the Agulhas Retroflection, as well as Circumpolar Deep Water flowing over the northern Agulhas Plateau. Furthermore, the northern slope of the Agulhas Plateau lies under the influence of North Atlantic Deep Water and Antarctic Bottom Water, both of which shape sediment drifts. Site U1582 is located on the flank of one of those basement highs (37°1.5002′S, 24°59.7168′E) at 3400 m water depth, where a small ledge is formed (Figure **F1**). The seismic data show basement

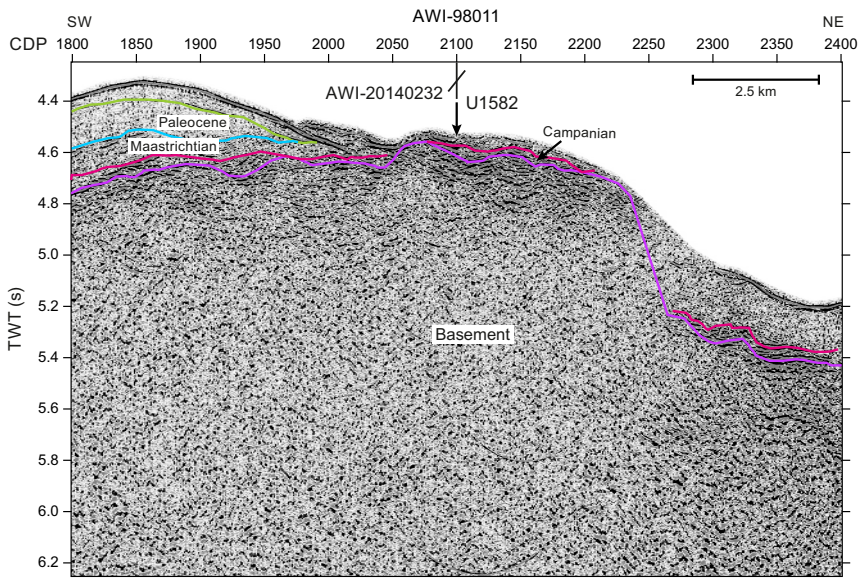

Figure F1. Seismic Line AWI-98011 showing Site U1582. Preliminary interpretation of seismic units according to the chronostratigraphic model is shown. The marked purple reflection corresponds in structure to the top of basement (see Figure F4 in the Expedition 392 summary chapter [Uenzelmann-Neben et al., 2023b]), the magenta reflection to Reflector M, the blue reflection to Reflector LE, and the green reflection to Reflector LO. CDP = common depth point, TWT = two-way traveltime.

below an ~100 m thick sedimentary sequence, which is characterized by Reflectors M and LE (see **Background** in the Expedition 392 summary chapter [Uenzelmann-Neben et al., 2023b]). The uppermost part of the basement further shows only a few internal reflections (Figure **F1**), which differs from the seismic character of the basement at Sites U1579 and U1580. This has been interpreted to represent more homogeneous basalt at Site U1582.

Site U1582 was selected to recover both the thin Paleogene–Cretaceous sedimentary cover and basement samples. This site was especially dedicated to recover an extended record of basement material to unravel the nature of the basement and provide information on its age and geochemistry. Additional objectives include identifying potential late-stage magmatism and its effect on sedimentary sequences. Integration of seismic profiles with the drilling results will allow direct dating of the observed Seismic Unconformities M and LE and interpretation of their causes, and recovery of the sediment/basement interface will provide information on the age of the oldest sediments above the basement as well as the water depth and environment at the time of deposition. At this site, a thin sediment sequence from the mid-Cretaceous to mid-Paleogene was expected to be drilled, spanning the long-term climate transition from the Cretaceous greenhouse to potentially the early Paleogene. The recovery of basement rocks at this site on the northern Agulhas Plateau was expected to help address fundamental questions about the formation of this LIP.

2. Operations

Site U1582 hole locations, water depths, and the number of cores recovered are listed in Table **T1**. All times are provided in local ship time (UTC + 2 h).

2.1. Hole U1582A

The vessel arrived at Site U1582 at 1420 h on 27 March 2022. The thrusters were lowered starting at 1424 h, the vessel was switched from cruise to dynamic positioning (DP) mode at 1440 h, and the rig floor was given the all clear. A new C-7 bit with a mechanical bit release was made up, and a four-stand rotary core barrel (RCB) bottom-hole assembly (BHA) was run into the hole starting at 1645 h. The drill pipe was lowered to 3378.3 meters below rig floor (mbrf), the sinker bars were installed, and the RCB system was deployed.

The first coring attempt at 2340 h resulted in a water core. Starting on 28 March, four more attempts were made to get the first core. On the sixth attempt, Hole U1582A was spudded at 0405 h, recovering Core 1R (recovery = 1.9 m). The seafloor was established at 3429.4 meters below sea level (mbsl). Coring continued, and basement was reached at 42.7 m core depth below seafloor, Method A (CSF-A). Half-cores were taken on Cores 6R and 7R. The final core for Hole U1582A, Core 7R, was cored to 48.0 m CSF-A, but more than 100% was recovered (48.68 m CSF-A). Coring was terminated at 1915 h to trip out of the hole because severe weather was expected over the site within 24 h.

The pipe was tripped out of the hole, clearing the seafloor at 1945 h. On 29 March at 0215 h, the pipe trip was completed with the BHA at the rig floor. The bit cleared the rig floor at 0455 h, ending Hole U1582A. The rig floor was secured at 0600 h, and the vessel was switched to cruise mode at 0604 h. The thrusters were raised and secured by 0618 h, and the sea passage for waiting on weather began with the vessel transiting north at 10.6 kt. The vessel turned and took a westerly heading at 1818 h. Beginning on 31 March, the vessel turned on a southerly and then easterly course to return to Site U1582.

A total of seven cores were taken in Hole U1582A over a 48 m interval (recovery = 38.5%). Total time on Hole U1582A was 38.16 h (1.59 days).

2.2. Hole U1582B

On 1 April 2022, the vessel arrived back at Site U1582. The thrusters were lowered starting at 1228 h, and the ship was switched to DP mode at 1245 h, ending the waiting on weather. The vessel was positioned 10 m west of Hole U1582A.

A new C-7 RCB bit was made up, and the BHA and pipe were tripped to the seafloor. A core barrel with a center bit was dropped, and Hole U1582B was spudded at 2315 h on 1 April. Seafloor was set at 3440.7 mbrf. The driller then proceeded to drill down before reaching a hard contact at 36.3 m CSF-A. The center bit was retrieved, and coring began at approximately 0530 h on 2 April; Core 2R was on deck at 1100 h. The rate of penetration was very slow, averaging just over 1 m/h, because the hard basalt formation and shallow depth of the hole limited how much weight could be put on the bit. Coring continued into 3 April, through Core 5R at a final depth of 55.6 m CSF-A (recovery to 53.73 m CSF-A).

The weather over the site was expected to deteriorate over the next 2 days, forcing us off site and into an early transit to Cape Town, South Africa. Coring was terminated at 0230 h on 3 April, and the pipe was tripped back to the vessel. The bit cleared the rig floor at 1250 h, ending Hole U1582B and Site U1582. The vessel was switched to cruise mode at 1236 h, the thrusters were raised and secured by 1249 h, and we began our sea passage to Cape Town, South Africa, at 1250 h with the vessel making a wide turn northwest. A total of four cores were taken in Hole U1582B over a 19.3 m interval (recovery = 52.2%). Total time on Hole U1582B was 48 h (2.0 days).

Expedition 392 officially ended with the first line ashore at 1154 h on 7 April 2022.

Table T1. Core summary, Site U1582. DRF = drilling depth below rig floor, DSF = drilling depth below seafloor, APC = advanced piston corer, HLAPC = half-length APC, XCB = extended core barrel. R = RCB. **Download table in CSV format.**

Hole U1582A
Latitude: 37°1.5002′S
Longitude: 24°59.7168′E
Water depth (m): 3429.36
Date started (UTC): 1245 h; 27 Mar 2022
Date finished (UTC): 0300 h; 29 Mar 2022
Time on hole (days): 1.59
Seafloor depth DRF (m): 3440.7
Seafloor depth est. method: Tag
Rig floor to sea level (m): 11.34
Penetration DSF (m): 48
Cored interval (m): 48
Recovered length (m): 18.48
Recovery (%): 39
Drilled interval (m): NA
Drilled interval (no.): 0
Total cores (no.): 7
APC cores (no.): 0
HLAPC cores (no.): 0
XCB cores (no.): 0
RCB cores (no.): 7
Other cores (no.): 0

Hole U1582B
Latitude: 37°1.5003′S
Longitude: 24°59.7114′E
Water depth (m): 3429.36
Date started (UTC): 1045 h; 01 Apr 2022
Date finished (UTC): 1045 h; 03 Apr 2022
Time on hole (days): 2
Seafloor depth DRF (m): 3440.7
Seafloor depth est. method: Offset
Rig floor to sea level (m):11.34
Penetration DSF (m): 55.6
Cored interval (m): 19.3
Recovered length (m): 10.08
Recovery (%): 52
Drilled interval (m): 36.3
Drilled interval (no.): 1
Total cores (no.): 4
APC cores (no.): 0
HLAPC cores (no.): 0
XCB cores (no.): 0
RCB cores (no.): 4
Other cores (no.): 0

Core	Top depth drilled DSF (m)	Bottom depth drilled DSF (m)	Interval advanced (m)	Recovered length (m)	Curated length (m)	Core recovery (%)	Core on deck date (2022)	Core on deck time UTC (h)	Sections (*N*)
392-U1582A-									
1R	0.0	1.9	1.9	1.90	1.90	100	28 Mar	0220	3
2R	1.9	11.6	9.7	5.78	5.78	60	28 Mar	0300	5
3R	11.6	21.3	9.7	4.11	4.11	42	28 Mar	0400	4
4R	21.3	31.0	9.7	0.46	0.46	5	28 Mar	0600	2
5R	31.0	40.7	9.7	0.83	0.83	9	28 Mar	0755	1
6R	40.7	45.5	4.8	2.61	3.17	54	28 Mar	1240	3
7R	45.5	48.0	2.5	2.79	3.18	112	28 Mar	1700	3
		Hole U1582A totals:	48.0	18.48	19.43				21
392-U1582B-									
11	0.0	36.3	36.3	*****Drilled interval*****			2 Apr	0330	0
2R	36.3	41.8	5.5	2.43	2.80	44	2 Apr	0900	3
3R	41.8	46.3	4.5	3.02	3.51	67	2 Apr	1405	3
4R	46.3	51.1	4.8	2.36	2.66	49	2 Apr	1855	2
5R	51.1	55.6	4.5	2.27	2.63	50	3 Apr	0010	2
		Hole U1582B totals:	55.6	10.08	11.60				10
		Site U1582 totals:	103.6	28.56	31.03				31

3. Lithostratigraphy

Site U1582 consists of a 40.92 m thick sequence of sediments overlying a 16.9 m interval of basalt with intercalated thin layers of sediment. The sedimentary succession is composed of nannofossil ooze, clayey silt, cobble-sized manganese nodules, and limestone. Carbonate content decreases from ~30% immediately below the seafloor in Sample 392-U1582A-1R-1, 82–83 cm (0.82 m CSF-A), to <5% in Sample 2R-1, 57–58 cm (2.47 m CSF-A), and it remains below 10% downhole to Sample 4R-CC, 4–5 cm (21.56 m CSF-A; deepest sample analyzed) (Figure **F2**). Lithostratigraphic unit and subunit boundaries at Site U1582 are largely defined using macroscopic core descriptions and smear slides and are supplemented by X-ray diffraction (XRD) analyses and physical properties (see **Physical properties**) and geochemical (see **Geochemistry**) data. Two lithostratigraphic units (I and II) are defined at Site U1582. Lithostratigraphic Unit I is divided into two subunits (Ia and Ib) (Figures **F2**, **F3**, **F4**; Table **T2**), and Lithostratigraphic Unit II consists of pillow basalts with interspersed limestone.

3.1. Lithostratigraphic Unit I

Interval: 392-U1582A-1R-1, 0 cm, to 6R-1A, 22 cm; 392-U1582B-2R-1, 0–53 cm
Depth: Hole U1582A = 0.00–40.92 m CSF-A; Hole U1582B = 36.30–36.83 m CSF-A
Age: upper Miocene–Turonian
Major lithologies: nannofossil ooze, clayey silt, clayey nannofossil ooze with sand, limestone, and manganese nodules

Lithostratigraphic Unit I is a ~40 m sequence of nannofossil ooze, clayey silt, and clayey nannofossil ooze with sand in the upper sections and limestone with manganese nodules at the base. Two lithostratigraphic subunits (Ia and Ib) are distinguished in Lithostratigraphic Unit I based on a downsection increase in lithification (Table **T2**). Both subunits contain variable amounts of sand, silt, clay, and manganese nodules. Magnetic susceptibility (MS) increases downcore starting in Lithostratigraphic Subunit Ia in Section 392-U1582A-2R-4 (~7 m CSF-A) and is variable in Lithostratigraphic Unit II (Figure **F2**). There are no obvious changes in components observed in smear

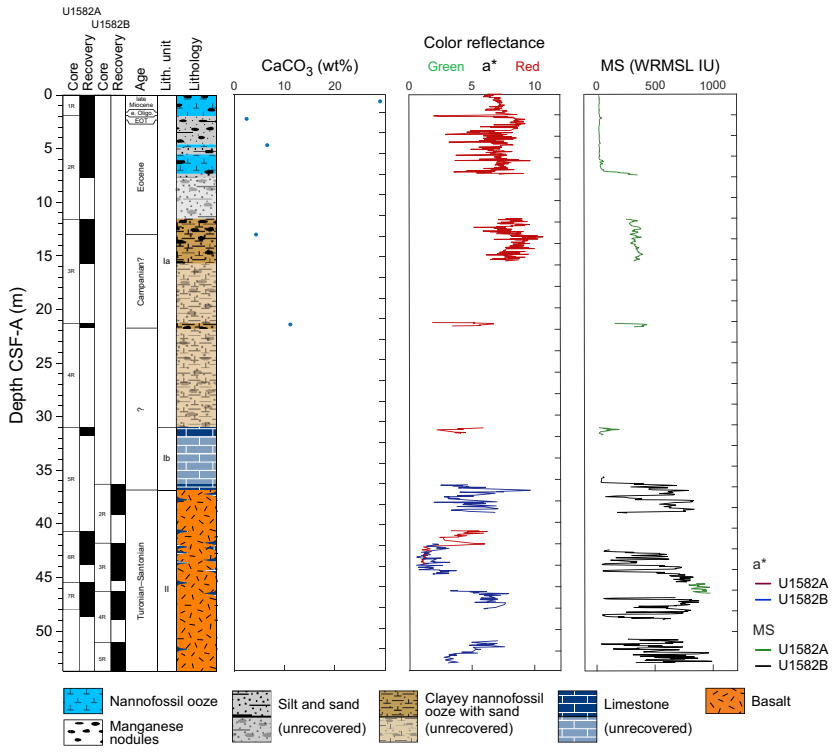

Figure F2. Lithostratigraphic summary, Site U1582.

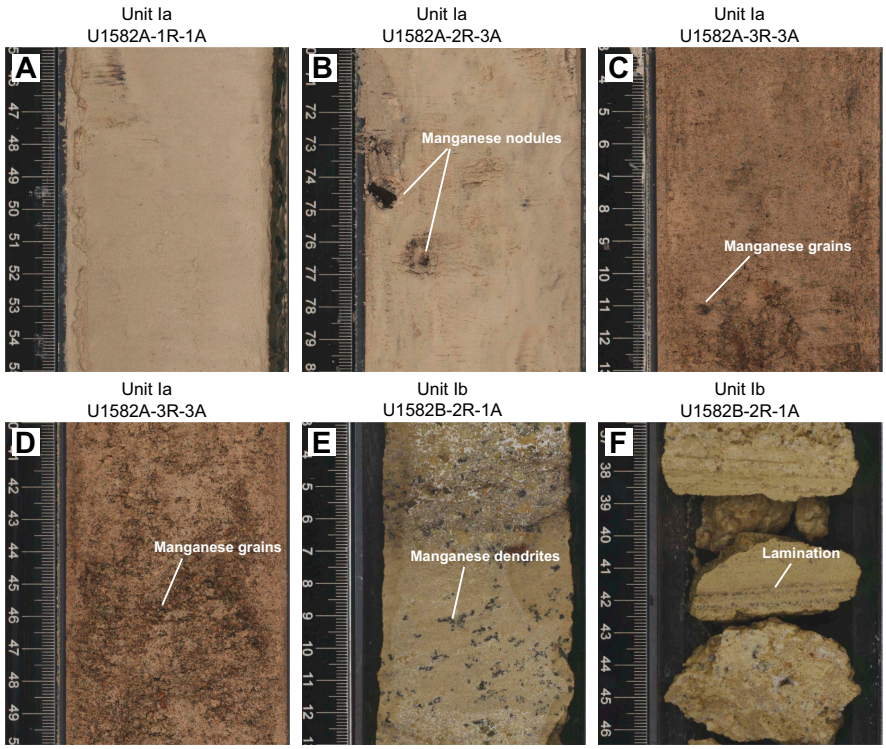

Figure F3. Major lithologies, Site U1582. A. Light yellowish brown and light brown nannofossil ooze (392-U1582A-1R-1, 45–55 cm). B. Light yellowish brown and light brown nannofossil ooze with manganese staining and nodules (2R-3, 70–80 cm). C. Light brown clayey nannofossil ooze with an increased proportion of sand and manganese nodules (3R-3, 3–13 cm). D. Light brown clayey nannofossil ooze with sand (3R-3, 40–50 cm). E. Pale yellow and light gray limestone with clasts and manganese dendrites (392-U1582B-2R-1, 3–13 cm). F. Pale yellow limestone with clasts and weak parallel lamination (2R-1, 36.5–46.5 cm).

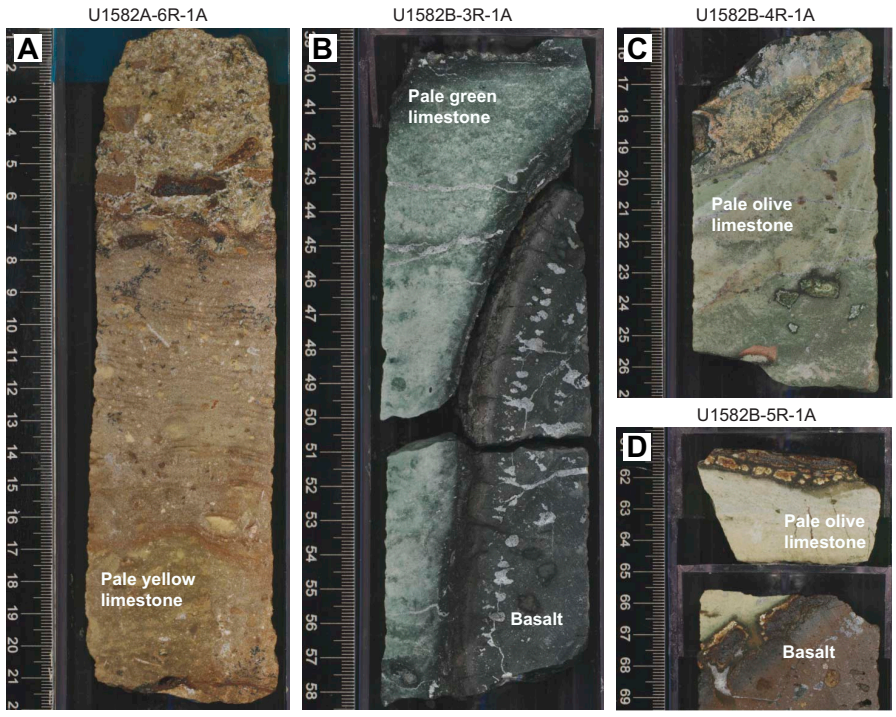

Figure F4. Intrabasalt sediments, Holes U1582A and U1582B. A. Pale yellow limestone with clasts (392-U1582A-6R-1, 1–22 cm). B. Pale green limestone (392-U1582B-3R-1, 38.5–58.5 cm). C, D. Pale olive limestone (4R-1, 15.2–27 cm, and 5R-1, 61.7–67 cm, respectively).

slides, carbonate content, color, or natural gamma radiation (NGR) associated with the downcore increase in MS; thus, we have not defined a new subunit at this transition. The Lithostratigraphic Subunit Ia/Ib contact is unclear because it occurs in an interval of poor recovery between Cores 4R and 5R (21.76–31.07 m CSF-A).

3.1.1. Lithostratigraphic Subunit Ia

Interval: 392-U1582A-1R-1, 0 cm, to 392-U1582A-4R-CC, 24 cm
Depth: 0.00–21.76 m CSF-A
Age: upper Miocene–Campanian(?)
Major lithologies: nannofossil ooze, clayey silt, clayey nannofossil ooze with sand, and manganese nodules

Lithostratigraphic Subunit Ia consists of light brown clayey silt, nannofossil ooze, clayey nannofossil ooze with sand, and manganese nodules (Figure **F5**). In interval 392-U1582A-2R-1, 10–20.5 cm (2.00–2.105 m CSF-A), there is a dark brown manganese nodule that is ~10 cm in diameter, and there are additional small nodules of manganese throughout the entire subunit. From Section 2R-4, 91 cm (7.32 m CSF-A), to the base of the subunit, medium to coarse sand-sized and occasionally pebble-sized manganese nodules occur. Smear slides from this unit yielded various proportions of quartz, feldspar, mica, and Fe-Mn oxides. Biogenic constituents include calcareous nannofossils, rare occurrences of foraminifera and trace amounts of sponge spicules (Figures **F6**, **F7**).

One bulk sediment XRD sample was taken in Lithostratigraphic Subunit Ia (392-U1582A-3R-1, 68–69 cm; 12.28 m CSF-A) in an interval of clayey nannofossil ooze with sand. The main mineral components in this sample are quartz, clinoptilolite (Ca), calcite, anorthite (feldspar), and montmorillonite + illite (Figure **F8**).

3.1.2. Lithostratigraphic Subunit Ib

Intervals: 392-U1582A-5R-1, 0 cm, to 6R-1A, 22 cm; 392-U1582B-2R-1, 0–53 cm
Depths: Hole U1582A = 31.07–40.92 m CSF-A; Hole U1582B = 36.30–36.83 m CSF-A
Age: Campanian(?)–Turonian
Major lithologies: limestone and manganese nodules

Table T2. Unit and subunit boundaries, Site U1582. **Download table in CSV format.**

Lith. unit	Generalized lithology	Hole U1582A Depth CSF-A (m)	Hole U1582A Core, section, interval (cm)	Hole U1582B Depth CSF-A (m)	Hole U1582B Core, section, interval (cm)
			392-U1582A-		392-U1582B-
Ia	Clayey nannofossil ooze, clayey silt, clayey nannofossil ooze with sand and manganese nodules	0.00–21.76	1R-1, 0, to 4R-CC, 24		
Ib	Limestone and manganese nodules	31.07–40.92	5R-1, 0, to 6R-1, 22	36.30–36.83	2R-1, 0, to 2R-1, 53
II	Pillow basalt with intercalated limestone	40.92–48.68	6R-1, 22, to 7R-3, 34	36.83–53.73	2R-1, 53, to 5R-2, 130

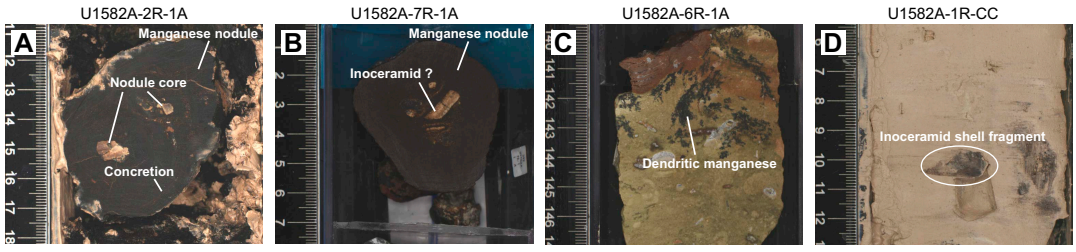

Figure F5. A. Manganese nodule (392-U1582A-2R-1, 11.2–17.5 cm). B. Manganese nodule with a possible inoceramid (bivalve) shell fragment at the center (7R-1, 0.8–6 cm). C. Manganese dendrites showing branching appearance on the surface of limestone (6R-1, 139–147 cm). D. Inoceramid shell fragment (1R-CC, 10 cm).

The light gray limestone and pale yellow limestone contain clasts of altered basalt and carbonate intraclasts, including pebble-sized angular calcite crystals. In the light gray limestone, manganese dendrites are present. The Lithostratigraphic Unit I/II contact was not recovered.

3.2. Lithostratigraphic Unit II

Intervals: 392-U1582A-6R-1, 22 cm, to 7R-3, 34 cm; 392-U1582B-2R-2, 0 cm, to 5R-2A, 130 cm
Depths: Hole U1582A = 40.92–48.68 m CSF-A; Hole U1582B = 36.83–53.73 m CSF-A
Age: Turonian/Santonian
Major lithology: basalt with intercalated limestone

Lithostratigraphic Unit II (Igneous Units 1–27) is 16.9 m in thickness and consists largely of pillow basalts with thin intercalated intervals of sediments (limestone and volcaniclastic material) (Figure **F4**). The sediments consist of pale yellow, light brown, and light grayish green limestone. In the pale yellow and light brown limestone, limonite is present at contacts with the basalt. Dendritic manganese and calcite veins are present in the limestone. Pale yellow limestones are present in Sections 392-U1582A-6R-1 (106–109 and 139–150 cm) and 392-U1582B-2R-2 (9–15, 23–34, 37–44, and 94–124 cm). Pale green limestones are present in Sections 392-U1582A-6R-2 (49–57 cm), 392-U1582B-3R-1 (15–22, 39–62, and 68–86 cm), and 3R-2 (23–25, 50–75, and 126–127.5 cm). Pale olive limestones are present in Sections 4R-1 (14–28 cm) and 5R-1 (62–66 cm). There is a cobble-sized manganese nodule in interval 392-U1582A-7R-1, 0–7 cm (45.50–45.57 m CSF-A) (Figure **F5**).

Volcaniclastic material is present in interval 392-U1582B-4R-2, 58–88 cm (see **Igneous petrology**).

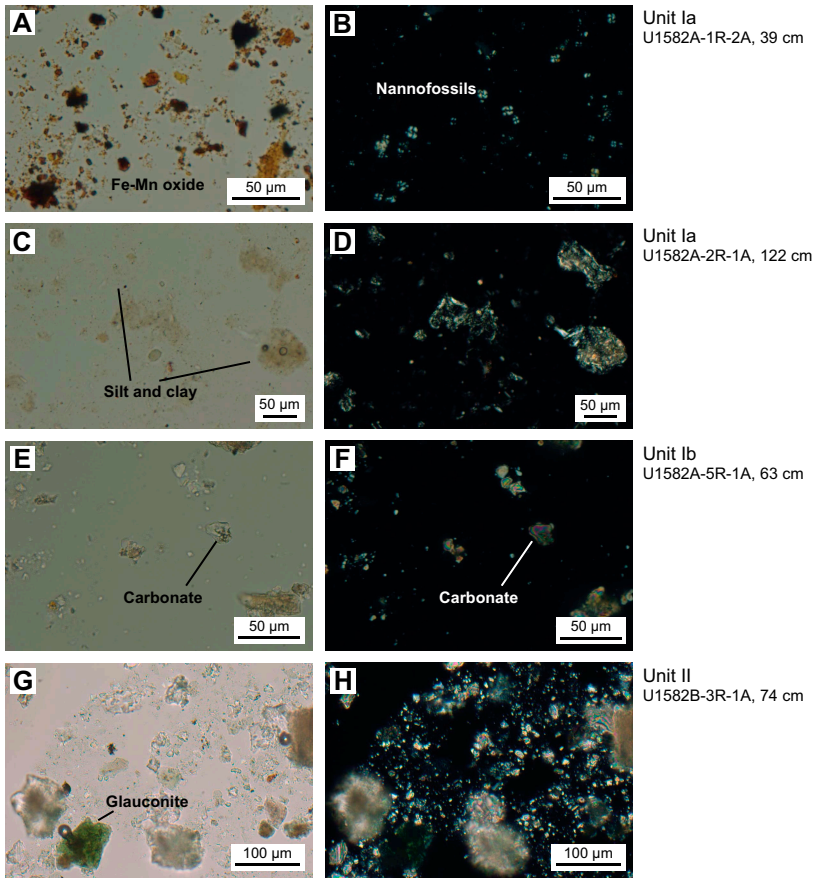

Figure F6. Major sedimentary lithologies, Site U1582. Left: plane-polarized light (PPL), right: cross-polarized light (XPL).

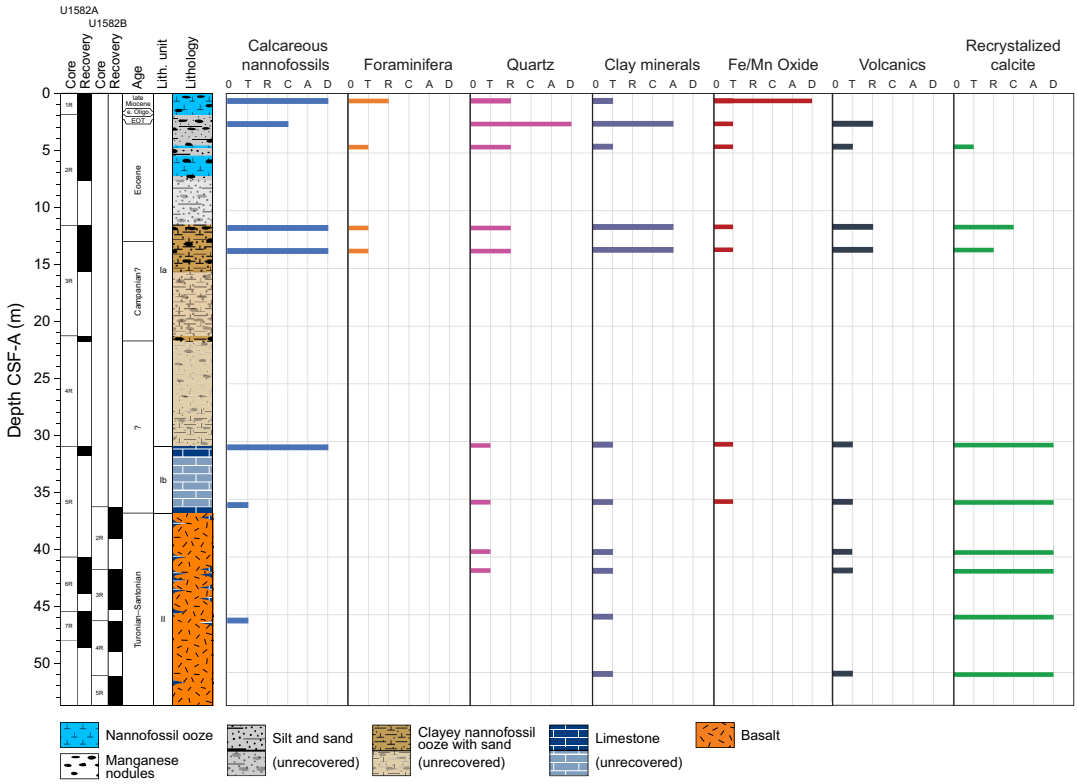

Figure F7. Main sedimentary component abundance compilation, Site U1582. 0 = not present, T = trace (0%–1%), R = rare (1%–10%), C = common (10%–25%), A = abundant (25%–50%), D = dominant (>50%).

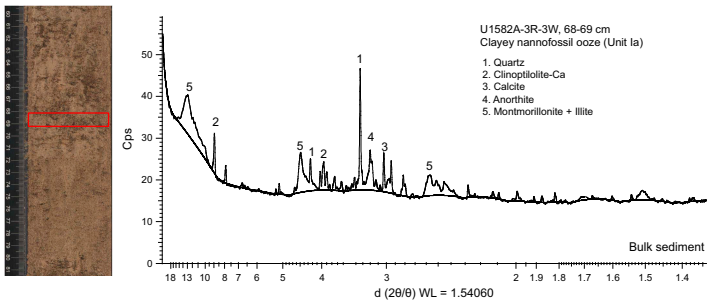

Figure F8. Bulk sediment XRD in the clayey nannofossil ooze of Lithostratigraphic Subunit Ia, Hole U1582A. Dominant minerals are clinoptilolite-Ca, quartz, anorthite (feldspar), calcite, and montmorillonite + illite (mixture).

4. Igneous petrology

4.1. Hole U1582A

Igneous rocks were first reached in Hole U1582A at 40.92 m CSF-A (Section 6R-1, 22 cm) below sedimentary Lithostratigraphic Subunit Ib (see **Lithostratigraphy**; Figure **F9**). A 7.76 m thick sequence of pillow lava basalts was penetrated until drilling ceased at 48.68 m CSF-A (Section 7R-3, 34 cm). Thirteen igneous units were identified and defined as individual inflationary pillow lava lobes (Table **T3**). Any sedimentary material in this succession is thin (<10 cm) and present as pockets of (carbonate) sediment that occupy interstices between individual pillow lobes (e.g., upper left corner of Figure **F10**). These interpillow sediments were therefore not considered separate lithostratigraphic units, and the entire pillow lava stack is therefore defined as Lithostratigraphic Unit II.

4.2. Lithostratigraphic and igneous units

4.2.1. Lithostratigraphic Unit II

Interval: 392-U1582A-6R-1, 22 cm, to 7R-3, 34 cm
Depth: 40.92–48.68 m CSF-A
Lithology: plagioclase phyric basalt and carbonate sediment
Igneous units: 1–13

Lithostratigraphic Unit II (Igneous Units 1–13; see Table **T3** for the intervals of the individual igneous units) comprises predominantly plagioclase phyric pillow basalts.

Igneous Unit 1, of which two separate fragments were recovered (Section 392-U1582A-6R-1 [Pieces 2 and 3]), comprises a single pillow lobe. Piece 2 contains a rounded rim that runs lengthwise within the core and a well-preserved chilled glassy margin. There is abundant fresh glass along this chilled contact as well as an outer layer of palagonized (weathered) glass and possibly some sedimentary material. The basalt in the interior of the lobe is fine grained, moderately to highly altered, and sparsely plagioclase phyric. It is moderately vesicular with typical radially arranged vesicle trains inward of the chilled margin (caused by ponding and trapping of the exhaling gas phase). All of the vesicles are filled with calcite. Piece 3 contains another chilled margin with fresh glass, marking the lower edge of the lobe.

Igneous Unit 2 is a moderately to highly altered, fine-grained, sparsely plagioclase phyric basalt. Plagioclase occurs as microphenocrysts not much larger than the groundmass. The rock is moderately vesicular, and all of the vesicles are filled with calcite. The unit as a whole is a single pillow basalt lobe, but the upper margin was not recovered. The lower contact is defined by an aphanitic margin with rubble pieces (subsumed as Section 392-U1582A-6R-1 [Piece 7]) of altered glass and a small piece of yellow carbonate sediment.

Igneous Unit 3 consists of another slightly curved vertical pillow rim with chilled glassy margins (Section 392-U1582A-6R-1 [Pieces 8–11]). Although the margin contains abundant fresh glass, the interior of the rock is highly to completely altered. Below, an 11 cm interval of yellow carbonate sediment was recovered, the upper end of which is in contact with brown palagonite from the rim of the above Igneous Unit 3 pillow margin.

The common yellow brownish color of all rocks of these three igneous units in Section 392-U1582A-6R-1 denotes considerable weathering and oxidation. In contrast, the basaltic rocks of Igneous Units 4–9 (interval 6R-2, 0 cm, to 7R-2, 53 cm) are light gray, suggesting a different alteration history.

Igneous Unit 4 comprises several pieces representing a single pillow lobe. The rock is moderately plagioclase phyric, and the groundmass grain size grades from aphanitic to fine grained toward the center of the unit. The upper margin is not recovered, but the lower margin is contained in several fragments of a glassy margin in direct contact with light green carbonate. The irregularity of the

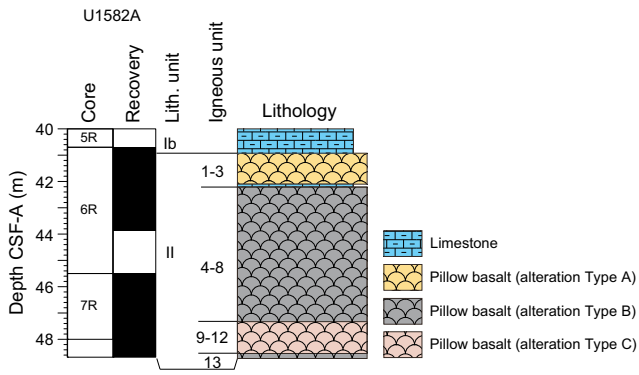

Figure F9. Stratigraphic summary, Hole U1582A.

lava/carbonate contact, signs of entrainment of the sediment within the lava (Section 392-U1582A-6R-2 [Piece 4]) (Figure **F11**), and fragments of lava and glass within sediment (Section 6R-2 [Piece 3]) all suggest mingling of the plastic lava with still unconsolidated (wet) sediment, a facies termed peperite (Skilling et al., 2002; see **Igneous petrology** in the Expedition 392 methods chapter [Uenzelmann-Neben et al., 2023a]).

Igneous Unit 5 is another pillow lobe denoted at the top by a chilled margin with fresh glass. A small piece of the green carbonate sediment mentioned above (between Igneous Units 4 and 5) is also attached to its rim, although it appears to crosscut the chilled margin, suggesting that the rock fractured after it cooled, allowing sediment to fill the void. Section 392-U1582A-6R-2 (Piece 6) of Igneous Unit 5 shows no contacts but appears to be the interior of this pillow, and vesicles near the

Table T3. Lithostratigraphic and igneous unit summary for rocks, Holes U1582A and U1582B. * = intervals with interpillow sediments. See text for explanation of alteration type divisions. **Download table in CSV format.**

Lith. unit	Igneous unit	Top core, section, interval (cm)	Top depth CSF-A (m)	Bottom core, section, interval (cm)	Bottom depth CSF-A (m)	Thickness (m)	Lithology	Alteration type
		392-U1582A-		392-U1582A-				
II	1	6R-1, 22	40.92	6R-1, 57	41.27	0.35	Plagioclase-phyric basalt	A
II	2	6R-1, 57	41.27	6R-1, 106	41.76	0.49	Plagioclase-phyric basalt	A
II	*	6R-1, 106	41.76	6R-1, 109	41.79	0.03	Carbonate sediment	
II	3	6R-1, 109	41.79	6R-1, 139	42.09	0.30	Plagioclase-phyric basalt	A
II	*	6R-1, 139	42.09	6R-1, 150	42.20	0.11	Carbonate sediment	
II	4	6R-2, 0	42.20	6R-2, 49	42.69	0.49	Plagioclase-phyric basalt	B
II	*	6R-2, 49	42.69	6R-2, 57	42.77	0.08	Carbonate sediment	
II	5	6R-2, 57	42.77	6R-2, 101	43.21	0.44	Plagioclase-phyric basalt	B
II	6	6R-2, 101	43.21	7R-1, 93	46.43	3.22	Plagioclase-phyric basalt	B
II	7	7R-1, 93	46.43	7R-1, 134	46.84	0.41	Plagioclase-phyric basalt	B
II	8	7R-2, 0	46.84	7R-2, 53	47.37	0.53	Plagioclase-phyric basalt	B
II	9	7R-2, 53	47.37	7R-2, 86	47.70	0.33	Aphyric basalt	C
II	*	7R-2, 86	47.70	7R-2, 92	47.76	0.06	Carbonate sediment	
II	10	7R-2, 86	47.70	7R-2, 111	47.95	0.25	Plagioclase-phyric basalt	C
II	11	7R-2, 111	47.95	7R-2, 150	48.34	0.39	Plagioclase-phyric basalt	C
II	12	7R-3, 0	48.34	7R-3, 14	48.48	0.14	Plagioclase-phyric basalt	C
II	13	7R-3, 14	48.48	7R-3, 34	48.68	0.20	Plagioclase-phyric basalt	B
		392-U1582B-		392-U1582B-				
II	1	2R-2, 0	36.83	2R-2, 98	37.81	0.98	Plagioclase-phyric basalt	A
II	2	2R-2, 98	37.81	2R-3, 80	39.10	1.29	Plagioclase-phyric basalt	A
II	3	3R-1, 0	41.80	3R-1, 16	41.96	0.16	Plagioclase-phyric basalt	B
II	4	3R-1, 16	41.96	3R-1, 40	42.20	0.24	Plagioclase-phyric basalt	B
II	5	3R-1, 40	42.20	3R-1, 68	42.48	0.28	Plagioclase-phyric basalt	B
II	*	3R-1, 68	42.48	3R-1, 86	42.66	0.18	Carbonate sediment	
II	6	3R-1, 86	42.66	3R-1, 123.5	43.04	0.38	Plagioclase-phyric basalt	B
II	7	3R-1, 123.5	43.04	3R-1, 131	43.11	0.08	Plagioclase-phyric basalt	B
II	8	3R-2, 0	43.11	3R-2, 50	43.61	0.50	Plagioclase-phyric basalt	B
II	*	3R-2, 50	43.61	3R-2, 62	43.73	0.12	Carbonate sediment	
II	9	3R-2, 62	43.73	3R-2, 88	43.99	0.26	Plagioclase-phyric basalt	B
II	10	3R-2, 88	43.99	3R-2, 104	44.15	0.16	Plagioclase-phyric basalt	B
II	11	3R-2, 104	44.15	3R-2, 125	44.36	0.21	Plagioclase-phyric basalt	C
II	*	3R-2, 125	44.36	3R-2, 127	44.38	0.02	Carbonate sediment	
II	12	3R-2, 127	44.38	3R-3, 25	44.66	0.28	Plagioclase-phyric basalt	C
II	13	3R-3, 25	44.66	3R-3, 90	45.31	0.65	Plagioclase-phyric basalt	C
II	14	4R-1, 0	46.30	4R-1, 17	46.47	0.17	Plagioclase-phyric basalt	C
II	*	4R-1, 17	46.47	4R-1, 28	46.58	0.11	Carbonate sediment	
II	15	4R-1, 28	46.58	4R-1, 113	47.43	0.85	Nearly aphyric basalt	B
II	16	4R-1, 113	47.43	4R-1, 128	47.58	0.15	Plagioclase-phyric basalt	A
II	17	4R-1, 128	47.58	4R-1, 142	47.72	0.14	Nearly aphyric basalt	A
II	18	4R-1, 142	47.72	4R-1, 150	47.80	0.08	Plagioclase-phyric basalt	A
II	19	4R-2, 0	47.80	4R-2, 30	48.10	0.30	Plagioclase-phyric basalt	A
II	20	4R-2, 30	48.10	4R-2, 58	48.38	0.28	Plagioclase-phyric basalt	A
II	21	4R-2, 58	48.38	4R-2, 88	48.68	0.30	Hyaloclastite breccia	
II	22	4R-2, 88	48.68	5R-1, 22	51.32	2.64	Plagioclase-phyric basalt	A
II	23	5R-1, 22	51.32	5R-1, 65	51.75	0.43	Plagioclase-phyric basalt	A
II	24	5R-1, 65	51.75	5R-1, 112	52.22	0.47	Plagioclase-phyric basalt	A
II	25	5R-1, 112	52.22	5R-2, 41	52.85	0.63	Plagioclase-phyric basalt	A/B (5R-2, 6)
II	26	5R-2, 41	52.85	5R-2, 101	53.45	0.60	Plagioclase-phyric basalt	B
II	27	5R-2, 101	53.45	5R-2, 125	53.69	0.24	Plagioclase-phyric basalt	B

top show a slight curvature that is possibly subparallel to a nearby margin where exsolving gases pooled. All vesicles are highly irregular and completely filled with calcite. The rock in this unit is fine grained with plagioclase microphenocrysts and sparse (total = <1%) larger phenocrysts as large as 4 mm.

Igneous Unit 6 is the thickest of all igneous units in Hole U1582A at 3.22 m, of which 1.60 m was recovered, including both the top and bottom margins. It is a fine-grained, plagioclase phyric basalt. The plagioclase phenocrysts are generally small microphenocryst glomerocrysts of 5%–8% abundance, although sparse (total = <1%), euhedral phenocrysts as large as 6 mm are also present. The rock is moderately to highly vesicular, and >90% of the vesicles are filled with calcite, including large (several centimeters) irregular-shaped gas blisters that likely formed by coalescence of much smaller vesicles. Despite its dark gray color and initial appearance of being relatively fresh, thin section observations show the rock is highly altered with most of the groundmass minerals replaced by clay minerals. Both the top and bottom of the unit are defined by curved chilled margins that contain fresh and altered glass, respectively.

Figure F10. Two pillow lava lobes (Igneous Units 10 and 11; 392-U1582A-7R-2). Solid red lines = curved chilled margins, dashed red lines = extrapolation of the margins. The rocks of Igneous Unit 11 show radial bands of vesicles trains (filled with white carbonate), which are typical for pillow lava lobes. Note the broad reddish brown oxidation halo running subparallel inward of the margins. A small piece of green carbonate sediment, visible at the top left of Igneous Unit 10, represents interpillow sediment.

Igneous Unit 7 is defined by chilled margins at both the top and bottom with altered glass at the top and abundant fresh glass at the bottom. It is a plagioclase phyric basalt with small needlelike microphenocrysts of plagioclase. The rock is moderately vesicular, and all vesicles are filled with calcite and only slightly altered.

Igneous Unit 8 is a plagioclase phyric basalt with small plagioclase microphenocrysts and very sparse (total = <1%) phenocrysts as large as 2 mm. The rock is highly altered (despite a relatively fresh macroscopic appearance and gray color), sparsely vesicular, and nearly all vesicles are filled with calcite. The top contact was not recovered, but the bottom of the unit is defined by a chilled margin with abundant fresh glass.

Igneous Units 9–12 in Sections 392-U1582A-7R-2 and 7R-3 are noticeably more (or at least differently) altered (reflected by an overall lighter gray surface color) than Igneous Units 4–8. Igneous Unit 9 is defined by chilled contacts both at the top and bottom, but only the bottom contact contains glass. The top contact is brecciated and shows contact with light green carbonate sediment, and a small piece of sediment is also in contact at its bottom margin. The unit is moderately vesicular, showing a bimodal size distribution with several (>10 mm) irregularly shaped vesicles filled with calcite and many smaller (≤1 mm) rounded vesicles that are mostly empty or filled with dark green or gray clay minerals. Aside from its overall light (bleached) color, signs of enhanced alteration include the presence of reddish (oxyhydroxite) schlieren and halos around veins and parallel to the chilled margins. In contrast to all other lava units of the igneous succession in Hole U1582A, this basalt is aphyric, although small microphenocrysts of plagioclase are present.

Igneous Unit 10 is moderately to highly altered and clearly defined by top and bottom chilled margins both with fresh glass and a contact with a small piece of light green carbonate (Figure **F10**). A reddish oxidation front running inward of the chilled margin is much wider (several centimeters) than in Igneous Unit 9, indicating a higher degree of oxidative alteration in these areas. Very similar to Igneous Unit 9, the vesicles are bimodal in size, and the small round vesicles remain unfilled, whereas the large irregular vesicles are filled completely with calcite. Those larger vesicles likely represent gas blisters. The groundmass of this sparsely plagioclase phyric basalt is fine grained and contains rare plagioclase microphenocrysts.

Igneous Units 11 and 12 are defined at both the top and bottom by chilled glassy margins. These sparsely plagioclase phyric basalts are highly altered with a broad oxidation front running inward of the chilled margins, similar to Igneous Unit 10. The rocks lack the bimodal vesicle distribution of Igneous Units 9 and 10, and all vesicles are filled with white calcite.

The lowermost Igneous Unit 13 is completely within Section 392-U1582A-7R-3 (Piece 2), which contains a near-vertical section through a pillow lobe with a chilled glassy margin at the top.

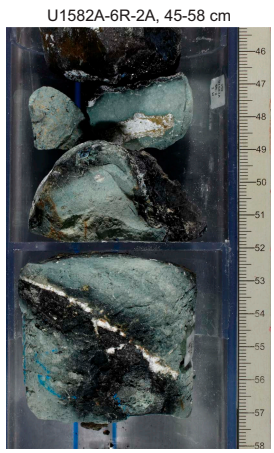

Figure F11. Irregular contact between glassy lava (dark) of Igneous Unit 4 and carbonate sediment (light green) suggesting mingling of plastic lava with still unconsolidated (wet) sediment, a facies termed peperite (392-U1582A-6R-2, 45–58 cm). Note the small enclave of sediment at 56–57 cm surrounded by a sharp glass (chilled) margin. The white strip is a secondary calcite filled vein, which formed after the rock solidified.

Again, the basalt is slightly plagioclase phyric with a grain size grading from glassy to aphanitic and finally fine grained toward the interior of the lobe. In contrast to the rocks of Igneous Units 9–12, this unit possesses a dark gray color and shows no signs of oxyhydroxite staining, indicating a much less developed state of oxidative weathering. In that respect, the rock resembles those of Igneous Units 4–8.

4.3. Hole U1582B

Hole U1582B was spudded 10 m west of Hole U1582A and recovered the same principal lithologies as Hole U1582A. Igneous rocks were first reached at 36.83 m CSF-A (Section 2R-2, 0 cm) below sedimentary Lithostratigraphic Subunit Ib (see **Lithostratigraphy**; Figure **F12**). A 16.9 m sequence of pillow lava basalts was penetrated until drilling ceased at 53.73 m CSF-A (Section 5R-2, 130 cm, which is 5 cm below the bottom of the lowermost igneous unit). The ~4 m shallower occurrence of the igneous basement in comparison to Hole U1582A attests to the considerable lateral variability of pillow lava flow fields, which likely created an uneven sediment-basalt topography at this site. In total, 27 igneous units were identified in Hole U1582B: 26 pillow lava units and 1 sequence of hyaloclastite breccia (Igneous Unit 21) (Table **T3**). The pillow lava units were defined as individual inflationary lava lobes. All sedimentary intervals are associated with the pillow basalts, so the entire succession was assigned as a single Lithostratigraphic Unit II, consistent with the division applied for Hole U1582A.

4.4. Lithostratigraphic and igneous units

4.4.1. Lithostratigraphic Unit II

Interval: 392-U1582B-2R-2, 0 cm, to 5R-2, 130 cm
Depth: 36.83–53.73 m CSF-A
Lithology: plagioclase phyric basalt and interpillow carbonate sediment
Igneous units: 1–27

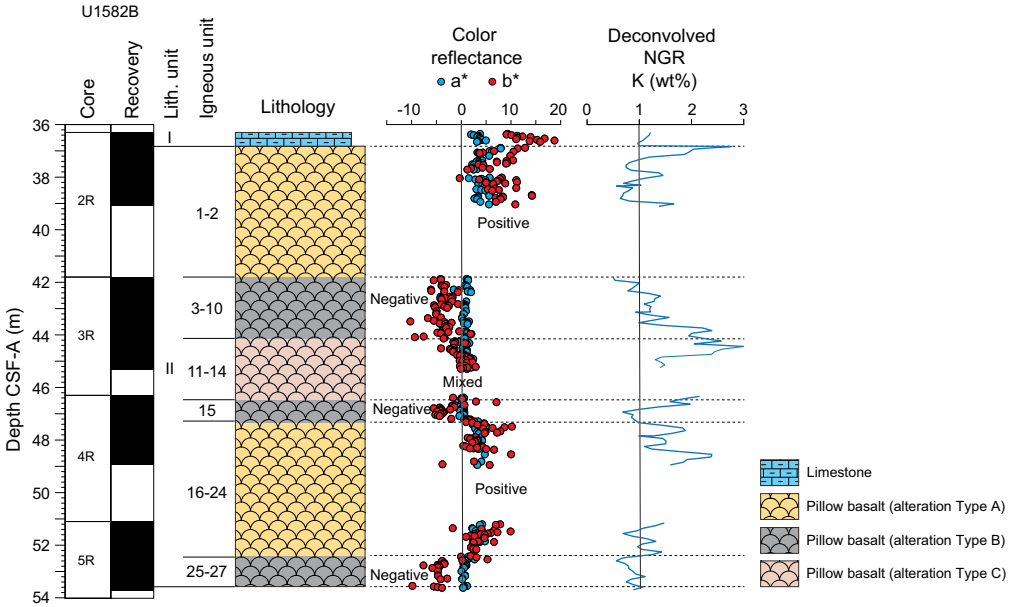

Figure F12. Stratigraphic summary, Hole U1582B. Physical properties data include color reflectance recorded relative to opponent color axes with a* (blue dots) displaying negative values toward green and positive values toward red and the b* (red dots) depicting negative numbers toward blue and positive values toward yellow. Accordingly, positive a*+b* values reflect a reddish brown color, corresponding to alteration Type A, and negative values reflect the gray color of alteration Type B. Deconvolved K content (in atomic weight percent) is inferred from NGR. Intervals of enriched K concentrations (predominantly >1 wt%) correspond to intervals with reddish brown alteration Type A (positive reflectance), whereas values around 1 wt% and below overlap with the gray alteration Type B (negative reflectance).

Lithostratigraphic Unit II (Igneous Units 1–27; see Table **T3** for the intervals of the individual igneous units) comprises predominantly plagioclase phyric pillow basalts. Because of the general lateral variability of pillow lava flow fields, an exact correlation of the uppermost igneous units recovered in Hole U1582B to the top of the pillow lava stack cored in Hole U1582A was not attempted. However, the uppermost part of the lava stack in Hole U1582B is characterized by the same alternation of alteration colors, switching between reddish brown (oxidized) and dark gray (reduced?) (see below).

Igneous Unit 1, which comprises Section 392-U1582B-2R-2 (Pieces 1–8), represents a large (diameter = >1 m) pillow lobe with a complex upper margin. Its glassy chilled margin meanders through the upper ~45 cm of this unit. Although the rock is moderately to highly vesicular, the irregular arrangement of the vesicles (e.g., no radially arranged vesicle trains) suggests a highly erratic shape of this inflation unit, which is consistent with its irregular upper margin. In that respect, Igneous Unit 2 is similar. The basalt of both Igneous Units 1 and 2 is moderately (3%–8%) plagioclase phyric and, except for the aphanitic region at the chilled margin, fine grained. Minor attachments of interpillow sediment in these two units are yellow brownish (e.g., in Section 2R-2 [Piece 3]).

Igneous Units 3–10 of Sections 392-U1582B-3R-1 through 3R-2 differ from the overlying igneous units by having a gray (and therefore apparently less oxidized) alteration color and generally smaller and more regularly shaped pillow lobes. In fact, the transition toward gray alteration color occurs in the uppermost part of Igneous Unit 3 in Section 3R-1, 4 cm. The rocks of these units are moderately to highly vesicular and generally show typical radially arranged vesicle trains inward of the chilled margin. Most of the larger (>3 mm) vesicles are filled with white calcite. Because of the generally smaller size of the individual inflation lobes in this portion of the lava stack, the rocks possess an aphanitic grain size that seldom reaches fine grained in the center of the few larger lobes. The basalts are moderately plagioclase phyric, and the absolute percentage of phenocryst content of 5%–10% is slightly higher than in Igneous Units 1 and 2. In marked contrast to the overlying units, all associated interpillow carbonate sediments in Igneous Units 3–11 are characterized by a turquoise greenish color (as opposed to bright yellowish brown in Igneous Units 1 and 2).

Igneous Unit 11 at the bottom of Section 392-U1582B-3R-2 marks the top of a more (pinkish) brownish sequence of pillow lavas that comprise Igneous Units 11–14. The basalts of these units are sparsely plagioclase phyric (3%–5%) and (except for their aphanitic margins) fine grained and highly vesicular. The vesicle fillings vary and include calcite (which generally fills the larger voids including gas blisters), clay minerals, and zeolites (the latter often appearing only as thin inner vesicle wall coatings).

An 11 cm piece of turquoise-green sediment (interval 392-U1582B-4R-1, 17–28 cm) separates the above units from the underlying Igneous Unit 15. This >80 cm large inflation lobe shows chilled and glassy upper and lower margins with grain size grading from aphanitic to fine grained toward the interior of the lobe. In contrast to most other lava units recovered in both holes at Site U1582, Igneous Unit 15 is nearly aphyric (<1% plagioclase phenocrysts). Interestingly, the alteration pattern fluctuates within this unit from reddish brown to gray, an observation that we revisit in the interpretation section below.

Igneous Units 16–20 consist of highly altered, brown pillow lobes. The groundmass of these is fine grained, and all but Igneous Unit 17 contain 3%–5% small plagioclase phenocrysts. The lavas are generally moderately vesicular with large elongated or irregular-shaped vesicles arranged concentrically around the edges of the pillows. These vesicles are mostly filled with calcite but also sometimes contain clays or other minerals. Most of these units also have small (~1 mm) round and unfilled vesicles.

Igneous Unit 21 is a 30 cm hyaloclastite breccia (interval 392-U1582B-4R-2, 58–88 cm). The highly fragmented clasts are mostly palagonitized (altered) volcanic glass fragments in a matrix of dark brown clay. Pillow lava successions are known to contain substantial amounts of hyaloclastite deposits consisting of glass shards (spalled off expanding pillows) and keystone-shaped rock fragments from pillow rims. Such rock fragments, with partly still preserved fresh glass, are prominent

in Section 4R-2 (Pieces 4 and 5). Within their rims, the bright orange palagonite fragments are replaced by white calcite. Section 4R-2 (Piece 6) bears the contact to Igneous Unit 22.

Igneous Units 22–24 are another succession of basaltic pillow lobes that are similar to Igneous Units 16–20 and have the same reddish brownish alteration color. Igneous Unit 22 in particular is nearly indistinguishable from Igneous Unit 20. Igneous Units 23 and 24 have more abundant plagioclase phenocrysts (as much as 10%) that are also slightly larger (as large as 2 mm). These two units are also a bit less vesicular with smaller average vesicle size. The basalts are all fine grained and highly altered. The units are defined by glassy chilled margins, some containing fresh glass. The top of Igneous Unit 24 in particular has abundant fresh glass and a small amount of interpillow carbonate sediment surrounding the pillow lobe.

Igneous Units 25–27 return again to the dark gray alteration color encountered in the overlying succession (except for the upper ~25 cm of Igneous Unit 25, which comprises the transition from reddish brown to gray color in interval 392-U1582-5R-2, 4–8 cm). The basalts of these units have a fine-grained groundmass and are moderately plagioclase phyric (like Igneous Units 23 and 24) with 8%–10% plagioclase phenocrysts as large as 2 mm, except for the deepest Igneous Unit 27, where plagioclase phenocrysts are smaller. All units are highly altered despite their fresh macroscopic appearance. They are also moderately vesicular with irregular vesicles mostly filled with calcite but some with clay and other secondary minerals (e.g., zeolites). All three units are defined by their chilled and glassy upper margins, which all contain fresh glass. However, the bottom margins were not recovered for any of these units.

4.5. Interpretation of the igneous units

Based on observed structures such as curved chilled margins and the presence of thick (fresh and altered) glass rinds along these margins, radially arranged vesicle trains, and concentric vesicle bands parallel to the curved margins, the entire igneous succession cored in Holes U1582A and U1582B is interpreted as a stack of pillow lava lobes. Pillow basalts are typical mafic submarine eruption products that form at relatively low effusion rates (e.g., Batiza and White, 2000). Although the individual lobes usually have relatively small diameters (≤1 m), larger inflation units such as the >3 m thick Igneous Unit 6 in Hole U1582A form by the same principal eruption process.

The presence and provenance of the pockets or intervals of interpillow carbonate sediment (e.g., in interval 392-U1582A-6R-2, 49–57 cm) (Figures **F10**, **F11**) often recovered in direct contact with the pillow rims is peculiar. These carbonates could represent (1) the seafloor substrate on or into which the pillow units were emplaced during eruption, (2) carbonate cemented former hyaloclastic material from the pillow rims (glass shards detached by contraction fragmentation) that was later recrystallized with calcite, (3) calcite precipitation out of heated seawater or hydrothermal fluids circulating through these void spaces shortly after eruption, or (4) accumulation of mainly carbonate-sedimentary material in the numerous interstices between the solidified pillow lobes significantly after eruption. Detailed postcruise thin section examination of the igneous/sediment contacts will help answer this question. However, the presence of microfossils in at least some of these carbonate pockets (see **Micropaleontology**) rules out a purely diagenetic origin of the carbonate. Instead, the evidence of plastic lava mingling with unconsolidated sediment (Section 6R-2 [Pieces 3 and 4]) (Figure **F11**) is tentatively interpreted as peperite, which implies an interaction of lava and coexisting sediment during eruption. Jordan et al. (2008) proposed a process whereby pillow lavas formed directly within shallow, unconsolidated sediment. Rapid quenching of the magma by water-saturated fine carbonate sediment could have provided conditions similar to those of lava extruding directly into water.

The repeated pattern of different styles of alteration is conspicuous in both holes. We have assigned these patterns to three types: A, B, and C (Table **T3**; Figures **F9**, **F12**). Type A is a reddish brown alteration indicative of an oxidizing environment. The transition of these alteration types sometimes runs through individual pieces in the interior of pillow units, such as in Sections 392-U1582B-3R-1, 4 cm (Piece 1), or 4R-1, 75–90 cm (Pieces 3c and 3b). Thin section examinations across this transition (interval 3R-1, 3–6 cm [TS30]) reveal that the clay minerals that have com-

pletely replaced the glassy mesostasis and pyroxenes in the groundmass show an orange color in the Type A part of the rock versus a dark gray color in the Type B part. The vesicles in the Type A portion are also filled with more reddish colored clay minerals compared to the Type B section.

Type B is a gray alteration that is likely indicative of a reducing environment. The gray color can be interpreted, at first glance, to mean that these rocks were not affected by significant alteration. On a closer inspection, particularly after thin section examination, it becomes evident that the gray color is maintained by abundant dark clay minerals (possibly saponite) replacing the groundmass phases and in particular most of the pyroxenes and mesostasis. Consistently, the carbonate sediments found between pillow lobes also seem to reflect the different alteration patterns. Carbonate in the reddish brownish alteration intervals of Type A has always a yellowish color, whereas carbonate in the gray alteration Type B succession shows exclusively a turquoise-green color.

The last identified type of alteration, Type C, is a mix between Types A and B, with lavas having a light gray to sometimes slightly pink or purple color. This type could represent a combination of the two other types of alteration. Examples of section-half images of intervals of the three alteration types are shown in Figure **F13**.

White calcite is abundant in all three alteration types, replacing pyroxene but rarely the groundmass and filling vesicles and veins. Likewise, the occurrence of fresh versus altered volcanic glass does not seem to correlate with the predominance of any of these alteration types. Most glassy margins of the Site U1582 basalts are rimmed by a soft black material that is apparently composed of a mixture of clay minerals. It is obvious that the intense alteration conditions in this pillow lava stack must have also impacted these margins, although coherent volumes of volcanic glass (like thick glassy pillow rims) are initially less affected by alteration because of their low permeability.

Interestingly, the three distinct alteration types differ in the percentage of K uptake (from seawater as part of the alteration process). Lavas belonging to the reddish brown Type A possess up to three times higher K content compared to the rocks of the gray alteration Type B (as deconvolved from NGR data; see **Physical properties**) (Figure **F12**). However, this does not seem to be the result of a greater extent of feldspar sericitization because thin section observations reveal that the plagioclase phenocrysts look similarly preserved in both Types A and B alteration, despite the near-complete alteration of the groundmass (Figure **F14**). Larger single-crystal phenocrysts of plagioclase are present in some samples as well as glomerocrysts of small (but still larger than the

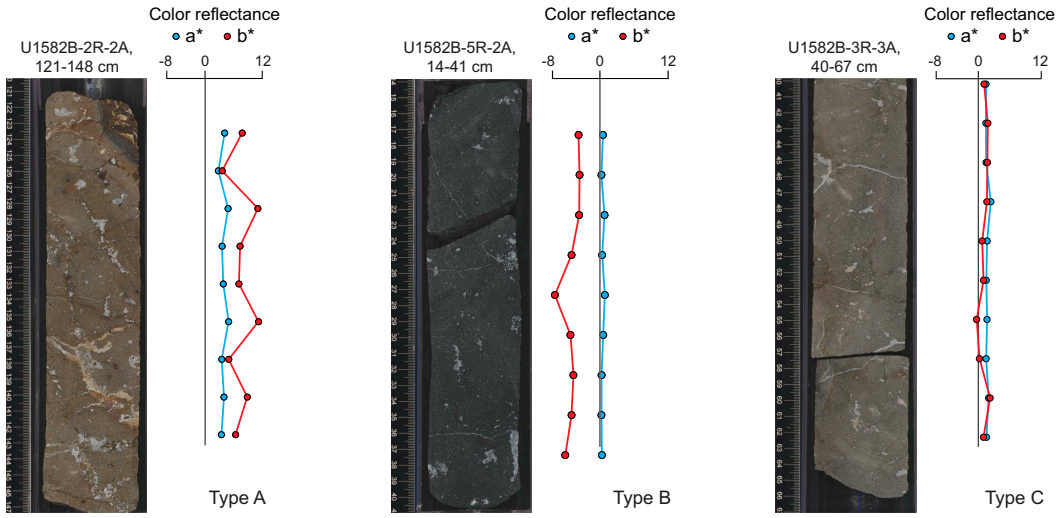

Figure F13. Examples of intervals displaying alteration Types A, B, and C with measured color reflectance data, Hole U1582B. These are recorded relative to opponent color axes with a* (blue dots) displaying negative values toward green and positive values toward red and the b* (red dots) depicting negative numbers toward blue and positive values toward yellow. Accordingly, positive a*+b* values reflect a reddish brown color, corresponding to alteration Type A, and negative values reflect the gray color of alteration Type B.

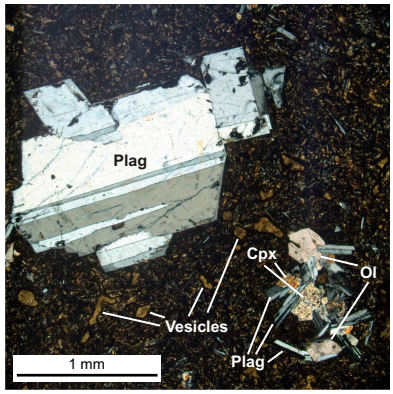

Figure F14. Large plagioclase (Plag) phenocryst and a glomerocryst of plagioclase, clinopyroxene (Cpx), and olivine (Ol) pseudomorphs (replaced with calcite) (392-U1582B-3R-1, 0–3 cm [XPL]). The surrounding groundmass is almost completely altered, and vesicles filled with clay minerals are also shown.

groundmass) plagioclase, clinopyroxenes, and olivine pseudomorphs (completely replaced with calcite; Figure **F14**).

It is also noteworthy to mention the similarity of the alteration style alternations with respect to absolute depth across holes at Site U1582. The principal transition between presumably oxidative (Type A) to reduced or suboxic conditions (Type B or C) occurs at 42.0 ± 0.2 m CSF-A (despite the ~4 m deeper onset of the igneous basement in Hole U1582A). Considering the lateral variability of any pillow lava flow field, this consistency is remarkable and suggests the existence of a widespread horizontal subseafloor oxidation front at some point in time. Alternatively, this concordance could just be a coincidence.

The biostratigraphically constrained Santonian to early Turonian age (83.6–93.7 Ma) of the interpillow carbonate sediments place these lavas several million years younger than the postulated formation age of the Agulhas Plateau based on seismic studies and plate tectonic reconstructions (95–105 Ma) (e.g., Gohl et al., 2011; Gohl and Uenzelmann-Neben, 2001). This means that either the reconstructions need to be revised or that the Agulhas Plateau aligns with several other large oceanic plateaus for which an emplacement duration longer than the canonical 1–2 My (e.g., Coffin and Eldholm, 2001) is substantiated. Alternatively, this pillow lava field belongs to a late rejuvenated or posterosional stage of volcanism, which must not necessarily be causally related to the bulk of Agulhas Plateau magmatism (e.g., Homrighausen et al., 2018). As outlined elsewhere (see **Igneous petrology** in the Site U1580 chapter [Bohaty et al., 2023]), such late-stage eruptions are usually characterized by alkaline composition. Preliminary shipboard portable X-ray fluorescence (pXRF) spectrometry analyses, however, indicate a tholeiitic composition for the Site U1582 pillow lavas, which is consistent with the composition of the only three available dredge samples from the Agulhas Plateau (Jacques et al., 2019). These samples were obtained from two dredge hauls that were conducted on the eastern and western slopes of the same basement high on which Site U1582 is located (~20 and ~24 km distant, respectively) and possess a tholeiitic (and enriched mid-ocean-ridge basalt) composition.

5. Micropaleontology

The 53.73 m thick succession at Site U1582 contains calcareous nannofossils and foraminifera in varying abundances. The sediment is barren of siliceous microfossils, and samples were not processed for palynomorphs due to the nature of the sediment, weather conditions, and time constraints near the end of the expedition. The sediment succession above basalt (Hole U1582A = 0–40.92 m CSF-A; Hole U1582B = 36.30–36.83 m CSF-A) primarily consists of nannofossil ooze with abundant manganese nodules together with clayey silt and sand (0–21.76 m CSF-A, Lithostratigraphic Subunit Ia; see **Lithostratigraphy**) overlying limestone (Lithostratigraphic Subunit Ib; Hole U1582A = 31.07–40.92 m CSF-A; Hole U1582B = 36.30–36.83 m CSF-A). The sequence is

highly condensed and dated to the Campanian(?) to late Miocene. Basalt was encountered at 40.92 m CSF-A in Hole U1582A and at 36.83 m CSF-A in Hole U1582B (Lithostratigraphic Unit II). The basalt shows clear pillow structures with pockets of intercalated sediment containing sparse nannofossils that indicate a Turonian–Coniacian age (see **Igneous petrology**).

Figure **F15** provides a comprehensive overview of the occurrence and preservation of nannofossils and foraminifera documented in the Site U1582 sediments. Calcareous nannofossils are abundant and moderately to poorly preserved in the nannofossil ooze of Lithostratigraphic Subunit Ia (0–21.76 m CSF-A). The clayey silt and clayey sand beds in this subunit are barren or nearly barren of nannofossils. Preservation decreases from the top of the hole down through Lithostratigraphic Subunit Ia. Nannofossils are very rare and poorly preserved in the limestone of Lithostratigraphic Subunit Ib (Hole U1582A = 31.07–40.92 m CSF-A; Hole U1582B = 36.30–36.83 m CSF-A). Nannofossils are present in rare to few numbers and moderately preserved in the greenish gray limestone intercalated with basalt, whereas they are rarer and show poorer preservation in the yellowish brown limestone. Foraminifera are present in the upper four cores (Samples 392-U1582A-1R-1, 0 cm, to 4R-CC, 19–24 cm; 0–21.71 m CSF-A; Lithostratigraphic Subunit Ia), and range in age from recent in the mudline sample (Sample 1R-1, 0 cm) to Cretaceous (Sample 4R-CC, 19–24 cm; 21.71 m CSF-A). Preservation of Cretaceous-aged foraminifera ranges from good (Sample 2R-CC, 5–10 cm; 7.63 m CSF-A) to poor (Sample 4R-CC, 19–24 cm; 21.71 m CSF-A).

5.1. Calcareous nannofossils

We examined all RCB sediment core catcher samples from Hole U1582A as well as additional samples from split core sections to establish a calcareous nannofossil biostratigraphic framework for the sediment above basalt recovered at Site U1582 (Table **T4**). We also sampled sediment intercalated with basalt from Holes U1582A and U1582B to provide an estimate for the age of the

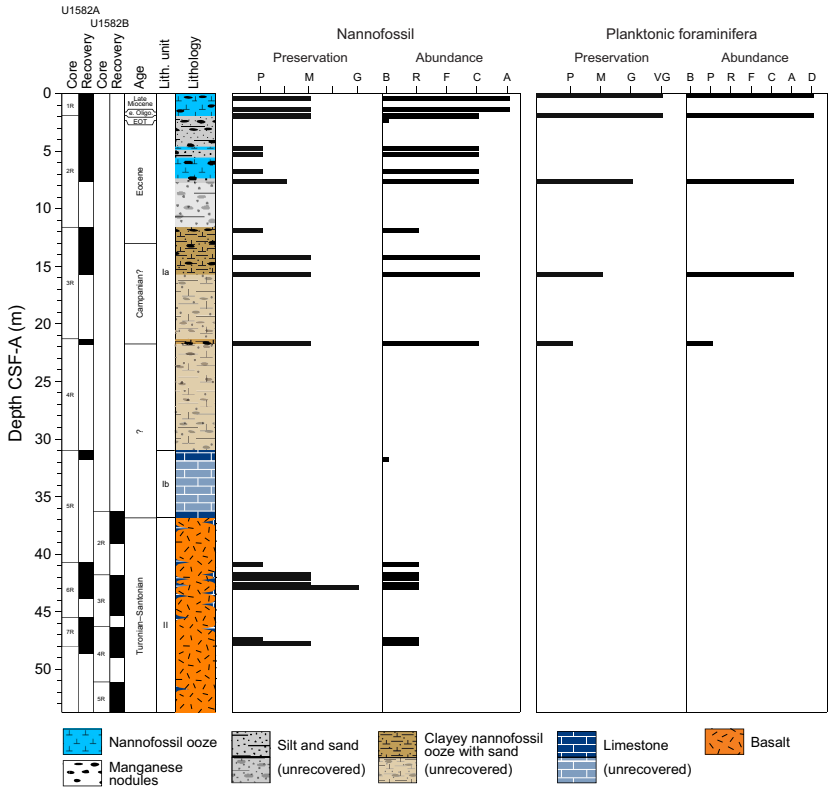

Figure F15. Overview of the preservation and abundance of nannofossils and planktonic foraminifera studied at Site U1582. Preservation: P = poor, M = moderate, G = good, VG = very good. Abundance: B = barren, P = present, R = rare, F = few, C = common, A = abundant, D = dominant. Nannofossil preservation: tick mark between P and M indicates poor–moderate preservation; tick mark between M and G indicates moderate–good preservation.

lava flows, which must be similar in age or older than the sediment. Calcareous nannofossil assemblage distribution data are based on shipboard observations, which focused on identification and tabulation of species that are age diagnostic; therefore, the recorded assemblage may not be fully representative of the entire nannofossil assemblage (Table **T5**). Photomicrographs of selected nannofossils from Site U1582 are shown in Figure **F16**.

The sediment section overlying basalt is only ~40 m thick at Site U1582, and the presence of abundant manganese nodules (see **Lithostratigraphy**) suggests low sedimentation rates, which are confirmed by nannofossil biostratigraphy. Lithostratigraphic Subunit Ia (0–21.76 m CSF-A) consists of nannofossil ooze, clayey nannofossil ooze, clayey silt, sand, and manganese nodules. Nannofossils are generally abundant through this subunit except in the silt and sand lithologies where nannofossils are sparse or absent. Preservation of Cenozoic nannofossils is moderate in Core 392-U1582A-1R and poor in Core 2R and the uppermost part of Core 3R. Cretaceous nannofossils in the lower part of Core 3R and the core catcher of Core 4R are moderately preserved (Figure **F15**). Nannofossils suggest that the sediment section is dated to the late Miocene to questionably the Campanian, although it is unclear if any of the Cretaceous material represents in situ deposition within Lithostratigraphic Subunit Ia. Significant mixing of assemblages is evident and is a result of reworking of older nannofossils into younger sediment, but there is also evidence of younger nannofossils in older sediment, which could be a result of burrowing or fall-in contamination due to coring disturbance in soft sediment near the seafloor. The latter is particularly likely for samples taken from near the tops of cores where fall-in can occur (see **Lithostratigraphy**). Nannofossils are rare to absent and poorly preserved in the limestone of Lithostratigraphic Subunit Ib (Hole U1582A = 31.07–40.92 m CSF-A; Hole U1582B = 36.30–36.83 m CSF-A). The sediment intercalated with basalt contains rare to few moderately preserved nannofossils, particularly in the greenish gray limestone, that indicate a Turonian–Coniacian age. The mixed assemblages and thin sediment section make it difficult to construct an age-depth model; however, we identify approximate ages for samples based on the youngest ages in the dominant assemblage (disregarding likely contamination) (Table **T4**).

Table T4. Biostratigraphic datums, Site U1582. Datum numbers correspond to those shown in Figure F21. B = base, T = top, X = crossover in abundance. For species with total range, the age is given as the midpoint age of its total range. **Download table in CSV format.**

Datum number	Datum	Age (Ma)	Top core, section, interval (cm)	Top depth CSF-A (m)	Bottom core, section, interval (cm)	Bottom depth CSF-A (m)	Midpoint depth CSF-A (m)
			392-U1582A-		392-U1582A-		
n1	*Discoaster quinqueramus* (total range: 5.53–8.13 Ma)	6.83	1R-1, 43	0.43	1R-2, 36	1.35	0.89
n2	B *Discoaster berggrenii*	8.29	1R-2, 36	1.35	—	—	1.35
n3	*Discoaster hamatus* (total range: 9.61–10.57 Ma)	10.09	1R-2, 36	1.35	—	—	1.35
n4	*Catinaster coalitus* (total range: 9.67–10.89 Ma)	10.28	1R-1, 43	0.43	1R-2, 36	1.35	0.89
n5	*Furcatolithus distentus* (total range: 26.81–30.00 Ma)	28.405	1R-CC, 14–19	1.85	—	—	1.85
n6	T *Furcatolithus predistentus*	26.93	1R-CC, 14–19	1.85	—	—	1.85
n7	T *Reticulofenestra umbilicus* >14 µm	32.02	1R-CC, 14–19	1.85	—	—	1.85
n8	T *Coccolithus formosus*	32.92	1R-CC, 14–19	1.85	—	—	1.85
n9	T *Isthmolithus recurvus*	33.06	2R-1, 8	1.98	—	—	1.98
n10	Common *Clausicoccus subdistichus* interval (range: 33.47–33.88 Ma)	33.675	2R-1, 8	1.98	—	—	1.98
n11	T *Discoaster saipanensis*	34.44	2R-1, 8	1.98	—	—	1.98
n12	T *Discoaster barbadiensis*	34.77	2R-1, 8	1.98	—	—	1.98
n13	*Nannotetrina cristata* (total range: 41.69–47.85 Ma)	44.77	2R-2, 131	4.71	2R-4, 35	6.76	5.74
n14	*Discoaster lodoensis* (total range: 48.22–53.58)	50.9	2R-2, 131	4.71	2R-4, 35	6.76	5.74
n15	*Tribrachiatus orthostylus* (total range: 50.65–54.30 Ma)	52.475	2R-2, 131	4.71	2R-4, 35	6.76	5.74
n16	X *Toweius* → *Reticulofenestra*	50.65	3R-1, 30	11.90	—	—	11.90
n17	*Uniplanarius trifidus* (total range: 71.31–76.77 Ma)	74.04	3R-2, 110	14.20	—	—	14.20
n18	*Reinhardtites anthophorus* (total range: 74.47–86.57 Ma)	80.52	3R-2, 110	14.20	4R-CC, 19–24	21.71	17.96
n19	B *Arkhangelskiella cymbiformis*	83.96	4R-CC, 19–24	21.71	—	—	21.71
n20	B *Reinhardtites anthophorus* (tentative)	86.57	6R-2, 48–49	42.68	7R-2, 89–90	47.73	45.21
n21	T *Eprolithus floralis*	84	6R-1, 106–107	41.76	—	—	41.76
n22	B *Eiffellithus eximius* s.l. (tentative)	90.36	6R-1, 106–107	41.76	6R-2, 48–49	42.68	42.22
n23	B *Eprolithus moratus*	93.73	6R-1, 140–141	42.10	U1582B-5R-1, 63–64	51.73	46.92

Table T5. Calcareous nannofossil distribution, Site U1582. **Download table in CSV format.**

5.1.1. Lithostratigraphic Unit I

Samples 392-U1582A-1R-1, 43 cm, to 3R-1, 30 cm (0.43–11.90 m CSF-A), contain Paleogene–Neogene assemblages, with reworked Cretaceous nannofossils present in some samples. All samples contain some degree of mixing; however, it is possible to derive approximate ages based on the youngest taxa in the predominant assemblage for most of this interval. Samples 1R-1, 43 cm (0.43 m CSF-A), and 1R-2, 36 cm (1.35 m CSF-A), contain a dominantly Neogene assemblage characterized by *Calcidiscus leptoporus*, *Calcidiscus tropicus*, *Umbilicosphaera rotula*, *Reticulofenestra* spp., *Discoaster exilis*, and *Discoaster variabilis* (Table **T5**). The youngest age-diagnostic taxa present are *Discoaster quinqueramus* (total range = 5.53–8.13 Ma; n1 in Figure **F21** and Table **T4**), *Discoaster berggrenii* (biohorizon base = 8.29 Ma; n2, same figure), *Discoaster hamatus* (total range = 9.61–10.57 Ma; n3, same figure), and *Catinaster coalitus* (total range = 9.67–10.89 Ma; n4, same figure). In addition, some late middle and early late Miocene nannofossils are also present, including *Coccolithus miopelagicus* (biohorizon top = 11.04 Ma), *Discoaster kugleri* (total com-

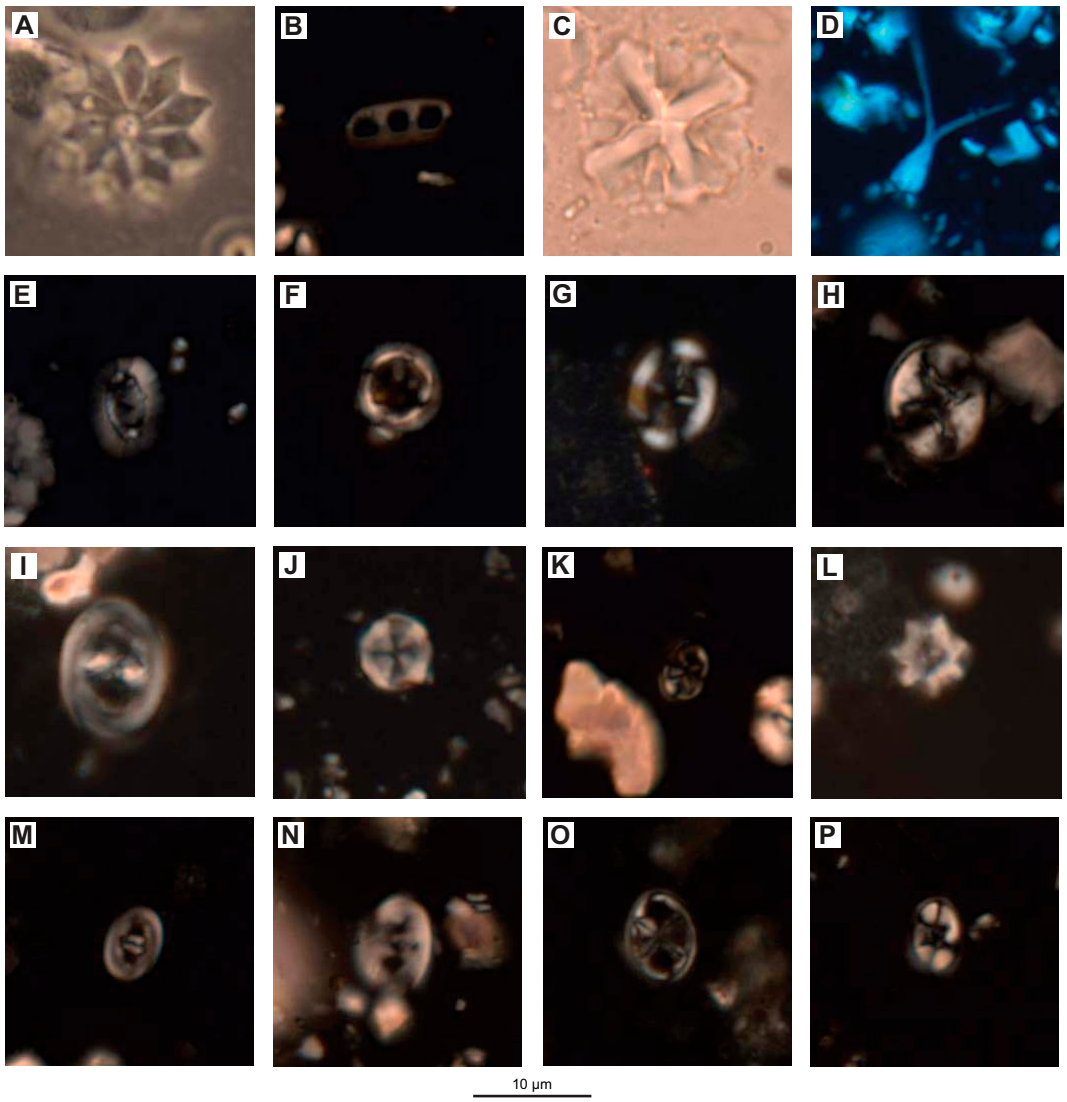

Figure F16. Selected calcareous nannofossils, Site U1582. Scale bar = 10 µm. (Parts A–L: Hole U1582A; M–P: Hole U1582B.) A. *Discoaster barbadiensis* (2R-1, 8 cm). B. *Isthmolithus recurvus* (2R-1, 8 cm). C. *Nannotetrina cristata* (2R-2, 131 cm). D. *Furcatolithus predistentus* (1R-CC). E. *Seribiscutum primitivum* (3R-2, 110 cm). F. *Stoverius achylosus* (3R-2, 110 cm). G. *Thiersteinia ecclesiastica* (4R-CC). H. *Eiffellithus eximius* sensu Verbeek (6R-1, 106 cm). I. *Reinhardtites anthophorus* (6R-2, 48 cm). J. *Radiolithus planus* (6R-2, 48 cm). K. *Helicolithus trabeculatus* (6R-2, 48 cm). L. *Eprolithus moratus* (6R-2, 71–72 cm). M. *Zeugrhabdotus bicrescenticus* (2R-2, 28 cm). N. *Tranolithus orionatus* (3R-2, 58 cm). O. *Chiastozygus platyrhethus* (3R-2, 58 cm). P. *Eiffellithus gorkae* (3R-2, 58 cm).

mon occurrence range = 11.61–11.89 Ma) in Sample 1R-1, 43 cm, and *Calcidiscus premacintyrei* (biohorizon top common = 12.57 Ma) in Sample 1R-2, 36 cm. We consider a single specimen of *Gephyrocapsa oceanica* found in the uppermost sample to be contamination or mixing from the seafloor. We assign a late Miocene age between ~5.5 and 10.9 Ma (Zones NN10–NN11 of Martini [1971]) to the interval between 0.43 and 1.35 m CSF-A).

Sample 392-U1582A-1R-CC, 14–19 cm (1.85 m CSF-A), contains a distinctly different assemblage characterized by *Cyclicargolithus floridanus*, Paleogene *Reticulofenestra* spp. (including *Reticulofenestra bisecta* >10 µm, *Reticulofenestra daviesii*, and *Reticulofenestra filewiczii*), and *Zygrhablithus bijugatus*. Age-diagnostic taxa include *Furcatolithus distentus* (total range = 26.81–30.00 Ma; n5, same figure), *Furcatolithus predistentus* (biohorizon top = 26.93 Ma; n6, same figure), *Reticulofenestra umbilicus* >14 µm (biohorizon top = 32.02 Ma; n7, same figure), and *Coccolithus formosus* (biohorizon top = 32.92 Ma; n8, same figure). These nannofossils suggest an early to mid-Oligocene age between ~26.8 and 33 Ma (Zones NP21–NP24) for this sample.

Sample 392-U1582A-2R-1, 8 cm (1.98 m CSF-A), was collected from nannofossil ooze above a large manganese nodule that may represent fall-in at the top of Core 2R (see **Lithostratigraphy**). The background assemblage is very similar to the Paleogene assemblage in Sample 1R-CC, 14–19 cm; however, a few specimens of Neogene taxa are present (e.g., *C. tropicus*, *D. exilis*, *D. variabilis*) and likely represent fall-in rather than a younger age based on the complete absence of other Neogene taxa. This sample contains common *Clausicoccus subdistichus* (n10, same figure) and *R. daviesii*, which have increased abundances in the earliest Oligocene immediately following the Eocene/Oligocene boundary (Backman, 1987; Fioroni et al., 2012). Other taxa present with biohorizon tops around the Eocene/Oligocene boundary include *Isthmolithus recurvus* (33.06 Ma; n9, same figure), *Discoaster saipanensis* (34.44 Ma; n11, same figure), and *Discoaster barbadiensis* (34.77 Ma; n12, same figure). Thus, we assign an age of latest Eocene to earliest Oligocene (~33–35 Ma; Zones NP19/20–NP21) for this sample.

Samples 392-U1582A-2R-2, 131 cm (4.71 m CSF-A), and 2R-3, 35 cm (5.25 m CSF-A), contain a poorly preserved nannofossil assemblage with many specimens preserved only as the outer rim of the coccolith. However, in both samples, some nannofossils are moderately preserved and allow identification to species level. These samples are characterized by common *Reticulofenestra* spp., *C. floridanus*, few specimens of *Toweius* spp., *Discoaster kuepperi*, and *Discoaster nodifer*. The age-diagnostic taxa include *Nannotetrina cristata* (total range = 41.69–47.85 Ma; n13, same figure), *Discoaster lodoensis* (total range = 48.22–53.58 Ma; n14, same figure), and *Tribrachiatus orthostylus* (total range = 50.65–54.30 Ma; n15, same figure). A single specimen of *I. recurvus* in Sample 2R-3, 35 cm, is considered contamination because other late Eocene–early Oligocene taxa are not present in the sample. We assign a very broad age of early to early middle Eocene between ~42 and 54 Ma (Zones NP10–NP16) to these samples. Sample 2R-4, 35 cm (6.76 m CSF-A), has a very similar assemblage except that it appears to have more Paleocene to earliest Eocene taxa, together with the early to early middle Eocene taxa present in the samples from Sections 2R-2 and 2R-3. Specifically, *Toweius* spp. are more abundant in this sample, whereas *Reticulofenestra* spp. are fewer in number; the abundance crossover of these two genera (n16, same figure) is dated to 50.65 Ma. Other taxa present in this sample include *Rhomboaster bramlettei* (biohorizon base = 56.0 Ma), *Heliolithus kleinpellii* (total range = 58.80–59.36 Ma), *Ellipsolithus bollii* and *Ellipsolithus macellus* (most abundant in the late Paleocene to earliest Eocene), and *Cruciplacolithus* spp. (including *Cruciplacolithus primus*, *Cruciplacolithus intermedius*, and *Cruciplacolithus tenuis*, which all have biohorizon bases in the early Paleocene). Although this sample is also assigned an early to early middle Eocene age (Zones NP10–NP16) based on the presence of *T. orthostylus*, *D. lodoensis*, and *N. cristata*, there is clearly mixing or reworking of upper Paleocene to lowermost Eocene sediment.

Samples 392-U1582A-2R-CC, 5–10 cm (7.63 m CSF-A), and 3R-1, 30 cm (11.90 m CSF-A), contain very mixed assemblages that we attribute to a combination of significant reworking of older material together with contamination from younger sediment resulting from coring disturbance (fall-in at the top of Core 3R and mixing in the core catcher of Core 2R). Both samples contain Cretaceous taxa interpreted as reworked, including *Biscutum constans*, *Eprolithus floralis*, *Eiffellithus eximius*, *Eiffellithus turriseiffelii*, *Kamptnerius magnificus*, *Prediscosphaera* spp., and

Watznaueria barnesiae. These samples also contain some Paleogene taxa found in the overlying samples, including *C. floridanus*, *Reticulofenestra* spp., *Chiasmolithus solitus*, *Coccolithus pelagicus*, and *Sphenolithus moriformis*. Sample 3R-1, 30 cm (11.90 m CSF-A) also contains a few specimens of Neogene taxa (*C. leptoporus*, *C. tropicus*, and *D. exilis*) that we interpret as contamination from fall-in. The mixed nature of the sediment makes it difficult to assign an age, but early (to early middle) Eocene similar to the overlying sample is consistent with the Paleogene taxa present in the samples.

Samples 392-U1582A-3R-2, 110 cm (14.20 m CSF-A); 3R-CC, 9–14 cm (15.66 m CSF-A); and 4R-CC, 19–24 cm (21.71 m CSF-A), contain a solely Cretaceous assemblage, although we cannot rule out that the entire assemblage is reworked into younger sediments. Nannofossils are common and moderately preserved in all three samples. The assemblage consists of frequent to common numbers of *B. constans*, *Eiffellithus* spp., *K. magnificus*, *Prediscosphaera cretacea*, *Seribiscutum primitivum*, *Tranolithus orionatus*, *W. barnesiae*, and *Zeugrhabdotus* spp. Age-diagnostic taxa include *Uniplanarius trifidus* (total range = 71.31–76.77 Ma; n17, same figure) in Sample 3R-2, 110 cm (14.20 m CSF-A), and *Arkhangelskiella cymbiformis* (biohorizon base = 83.96 Ma; n19, same figure) in Sample 4R-CC, 19–24 cm (21.71 m CSF-A). There is also a significant proportion of older (Coniacian Zones CC15–CC16) (Sissingh, 1977) nannofossils in these samples, including *E. floralis* (biohorizon top = 84.0 Ma; n21, same figure), *Lithastrinus septenarius* (biohorizon top = 85.30 Ma), *Quadrum gartneri* (biohorizon top = 85.09 Ma), and *Reinhardtites anthophorus* (biohorizon base = 86.57 Ma; n20, same figure). The lowermost sample (4R-CC, 19–24 cm; 21.71 m CSF-A) also contains *Thiersteinia ecclesiastica* (biohorizon top just above that of *L. septenarius* [Petrizzo et al., 2022]). The presence of *U. trifidus* and *A. cymbiformis* suggests a Campanian to earliest Maastrichtian age for these sediments. This interval is also dominantly reversed magnetic polarity (see **Paleomagnetism**), which suggests that the Samples from Core 3R were deposited during one of the reversed polarity chrons in the Campanian if the nannofossils represent in situ deposition.

Two samples from the limestone of Lithostratigraphic Subunit Ib (392-U1582A-5R-1, 80–83 cm [31.80 m CSF-A], and 6R-1, 18–19 cm [40.88 m CSF-A]), are either barren or contain very sparse and poorly preserved nannofossils of Cretaceous age. A single specimen of *R. bisecta* is likely contamination.

5.1.2. Lithostratigraphic Unit II

We sampled sediment within the basalt recovered at Site U1582 to give a first estimate for the age of the basalt, which must be contemporaneous with or older than the sediment. The sediment consists of two different colors of limestone: yellowish brown and greenish gray. Nannofossils are very rare in the yellowish brown limestone, whereas they are somewhat more abundant (rare to few numbers) and moderately preserved in the greenish gray limestone. The background assemblage is similar to that seen in the overlying sediment, including *B. constans*, *Eiffellithus gorkae*, *E. turriseiffelii*, *T. orionatus*, *W. barnesiae*, and various *Zeugrhabdotus* spp. There are also a number of taxa present that were either rare or not found in the overlying sediment, including *Chiastozygus litterarius*, *Nannoconus* spp., *Placozygus fibuliformis*, *Radiolithus planus*, *Repagulum parvidentatum*, and *Rhagodiscus angustus*. Both *E. floralis* (biohorizon top = 84.0 Ma; n21 in Figure **F21**) and *Eprolithus moratus* (biohorizon base = 93.73 Ma; n23, same figure) are consistently present and, taken together with age constraints from the overlying sediment, indicate a broad Santonian–Turonian age for the sediment (Figure **F21**; Tables **T4**, **T5**). Other age constraints come from single specimens of *E. eximius* s.l. (biohorizon base = 90.36 Ma; n22, same figure) found in three samples from Core 392-U1582A-6R, which constrain the age to mid-Turonian or younger if they are not contamination. Additionally, single specimens of probable *R. anthophorus* (biohorizon base = 86.57 Ma; n20, same figure) in two samples could further constrain the age to Coniacian or younger. The sparse nature of the assemblage and contamination observed in other samples from this site mean we prefer a broad age interpretation (Turonian to Santonian), which will have to be further investigated by postcruise research.

5.2. Foraminifera

Four core catcher samples and the mudline sample from Lithostratigraphic Subunit Ia of Hole U1582A were examined for foraminifera (Tables **T6**, **T7**). Preservation ranges from very good to

Table T6. Planktonic foraminifera distribution, Site U1582. **Download table in CSV format.**

Table T7. Benthic foraminifera distribution, Site U1582. **Download table in CSV format.**

poor in these samples (Sections 392-U1582A-1R-1 to 4R-CC; 0–21.71 m CSF-A). Sample 1R-1, 0 cm (0 m CSF-A), is dominated by planktonic foraminifera including *Trilobatus sacculifer*, *Globorotalia menardii*, *Globigerinella siphonifera*, *Globorotalia truncatulinoides*, *Neogloboquadrina dutertrei*, *Globoconella inflata*, *Globigerina bulloides*, and *Globoturborotalita apertura*. Planktonic foraminiferal abundances differ between the >150 and 63–150 µm size fractions of Sample 1R-CC, 14–19 cm (1.85 m CSF-A). The larger fraction (>150 µm) is made up of mostly *Catapsydrax unicavus*, *G. inflata*, and *G. apertura*, with some *Archaeoglobigerina australis*. The 63–150 µm fraction contains a greater abundance of the biserial *Planoheterohelix planata* and smaller *A. australis*, *Globorotaloides quadrocameratus*, *Globoturborotalita eolabiacrassata*, *Muricohedbergella sliteri*, *Planohedbergella aspera*, and *Planohedbergella prairiehillensis*, demonstrating mixing of Cenozoic and Mesozoic materials. Sample 1R-CC, 14–19 cm (1.85 m CSF-A), also contains large benthic foraminifera such as *Cibicidoides* and *Oridorsalis*. Sample 2R-CC, 5–10 cm (7.63 m CSF-A), has a higher abundance of Cretaceous species including *Gublerina cuvillieri* and *Archaeoglobigerina cretacea*, as well as the benthic foraminifera *Spiroplectammina spectabilis*. This interval also contains large (>200 µm) calcispheres, likely *Pithonella sphaerica*. Sample 3R-CC, 9–14 cm (15.66 m CSF-A), only contains common Cretaceous foraminifera including fairly well preserved *A. australis*, *A. cretacea*, and *M. sliteri*. Sample 4R-CC, 19–24 cm (21.71 m CSF-A), contains a significant gravel/pebble size fraction. Although calcite spar was noted in the 150–500 µm size fraction, foraminifera are rare, and preservation is poor in this sample.

6. Paleomagnetism

Paleomagnetic measurements were performed on all archive-half sections from Holes U1582A and U1582B (Cores 392-U1582A-1R through 7R, 0.0–48.68 m CSF-A; 392-U1582B-2R through 4R, 36.3–53.73 m CSF-A) and on four discrete samples from Cores 392-U1581A-1R through 3R and 7R (1.63–14.15 and 47.98 m CSF-A) (Figures **F17**, **F18**). No discrete samples were collected in Hole U1582B. Demagnetization experiments were performed to constrain a magnetic polarity stratigraphy for both holes.

Paleomagnetic measurements were undertaken on all archive halves from Holes U1582A and U1582B and on four discrete samples from Hole U1582A. Demagnetization experiments were performed on both sedimentary and igneous units recovered at Site U1582. Results indicate that the sampled units at Site U1582 are reliable recorders of magnetic field directions. Magnetic polarity was constrained from all measured cores. Intervals of both positive and negative inclination were identified in Hole U1582A, which is indicative of reversed and normal geomagnetic polarity, respectively (Figure **F17**). All measured cores from Hole U1582B had negative inclination (normal polarity) (Figure **F18**). Because of the condensed sediment interval collected in each hole, correlation to the geomagnetic polarity timescale (GPTS) (Ogg, 2020; Gradstein et al., 2020) was difficult; however, preliminary chron assignments were still made for Lithostratigraphic Unit II (Figures **F17**, **F18**).

6.1. Discrete samples

Discrete sediment and igneous rock samples were analyzed from Cores 392-U1582A-1R through 3R and 7R (1.63–14.15 and 47.98 m CSF-A). Because of poor recovery, no discrete samples were collected from Cores 4R or 5R. Additionally, to preserve important igneous structures (e.g., pillows), no discrete samples were collected from Core 6R. Alternating field (AF) demagnetization experiments were performed on all discrete samples starting at 5 mT with progressively increasing AF steps to a maximum field of 90 mT. This procedure was sufficient to reveal characteristic remanent magnetization (ChRM) directions for all four discrete samples. The quality of the demagneti-

zation data was high for all measured samples, and all four ChRM directions were determined using principal component analysis (Kirschvink, 1980) with the PuffinPlot software (Lurcock and Wilson, 2012) (Figure **F19**). All samples from the sedimentary Lithostratigraphic Subunit Ia were completely demagnetized by peak AF fields of 90 mT, which is indicative of a magnetic remanence held by low-coercivity ferrimagnetic minerals (e.g., magnetite) (Figure **F19A**). The one basalt sample analyzed (7R-3, 31 cm; 47.98 m CSF-A) was demagnetized completely after a maximum applied AF step of ~50 mT, which suggests that the remanence is carried by Ti-rich magnetite or large pseudosingle domain-like to multidomain size particles (Dunlop and Özdemir, 1997) (Figure **F19B**). All sedimentary samples have down-pointing directions (i.e., positive inclination), which indicates deposition during a reversed geomagnetic field. The one basalt sample has an up-pointing direction (i.e., negative inclination), which indicates deposition during a normal geomagnetic field. Because of the low number of samples, statistical analysis assessing whether the two polarities are antipodal could not be performed. Because of the limited amount of material recovered in Hole U1582A, rock magnetic experiments (like isothermal remanent acquisition) were not performed.

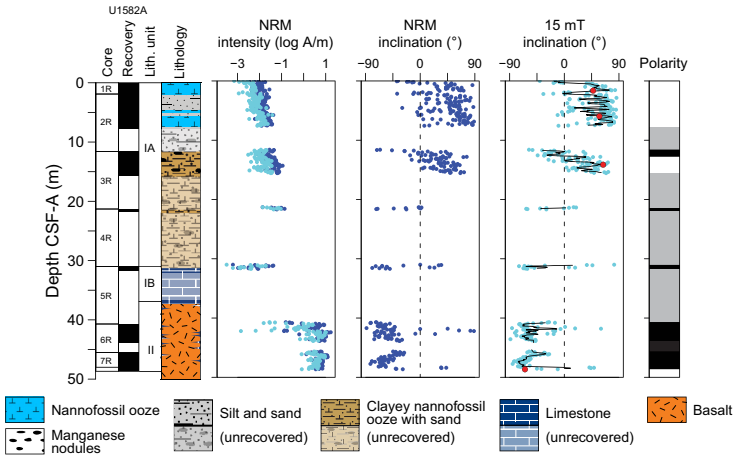

Figure F17. Magnetostratigraphic results, Hole U1582A. Dark blue dots = NRM intensity and inclination before AF demagnetization. Cyan dots = NRM intensity and inclination after 15 mT AF cleaning of the archive halves. Black line in inclination column = 5 point moving average, red dots = discrete samples. Magnetic polarity plot is generated from the moving average: negative (up-pointing) inclination indicates deposition during a normal geomagnetic polarity field (black bands). Gray bands = undetermined intervals (e.g., core gaps). In Hole U1582A, a reliable correlation with the GPTS was not possible.

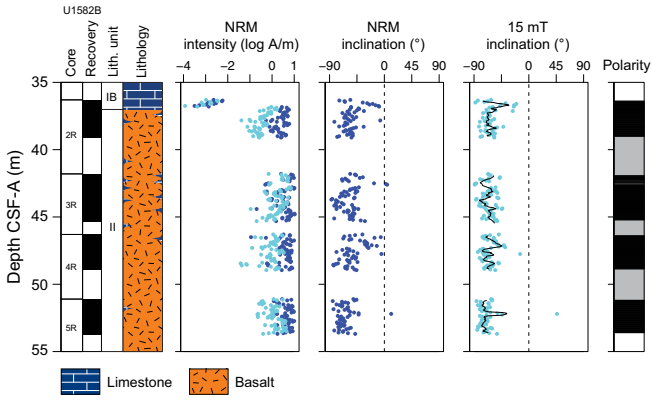

Figure F18. Magnetostratigraphic results, Hole U1582B. Dark blue dots = NRM intensity before AF demagnetization. Cyan dots = NRM intensity and inclination after 15 mT AF cleaning of the archive halves. Black line in inclination column = 5 point moving average. The magnetic polarity plot is generated from the moving average: negative (up-pointing) inclination indicates deposition during a normal geomagnetic polarity field (black bands). Gray bands = undetermined intervals (e.g., core gaps). In Hole U1582B, a reliable correlation with the GPTS was not possible.

6.2. Archive-half measurements

Downhole paleomagnetic natural remanent magnetization (NRM) measurements from Hole U1582A show a slight increase in magnetization intensity in Cores 1R–4R (0.0–21.76 m CSF-A) followed by a decrease in Core 5R (~31.0 m CSF-A). NRM intensity shows a marked increase of four orders of magnitude at the top of basaltic Lithostratigraphic Unit II (40.92 m CSF-A), which is sustained to the base of the hole (Figure **F17**). NRM intensity in Hole U1582B also shows a large increase of three orders of magnitude, straddling the contact between sedimentary Lithostratigraphic Subunit Ib and igneous Lithostratigraphic Unit II in Section 2R-2 (~36.8 m CSF-A) (Figure **F18**). This higher intensity is then sustained to the base of the hole. Archive halves from both holes were subjected to low-field AF demagnetization with maximum applied AF steps of either 15 or 20 mT. Full demagnetization experiments on discrete samples show that demagnetization to applied fields of 15 or 20 mT is sufficient to remove secondary overprints, providing a good approximation for the ChRM. All cores were RCB cored and not oriented. Therefore, polarity was determined from inclination values alone. A 5 point moving average was applied to measured inclination data to average out noise and help clarify polarity intervals. Stable magnetic directions were identified in all measured archive halves and were corroborated by discrete sample measurements. Measurements indicate that Cores 392-U1582A-1R through 3R (0–15.71 m CSF-A) have dominantly reversed polarity and Cores 4R–7R (21.3–48.68 m CSF-A) have normal polarity. Dual polarities are also readily observed in a histogram of inclination frequency throughout the hole (Figure **F20A**), with clear inclination peaks at ±65° (Figure **F20A**). A possible magnetic reversal from normal to reversed polarity is identified in Section 3R-1, 105–110 cm (12.65–12.7 m CSF-A); however, the inclination data are noisy, and it is difficult to confidently assign polarity. This interval may also be affected by drilling disturbance. In Hole U1582B, all measured archive halves have normal polarity, which is indicated by a single peak in inclination at ~65° (Figure **F20B**). All basaltic units in both holes have normal polarity (Cores 392-U1582A-6R through 7R and 392-U1582B-2R through 5R).

6.2.1. Magnetostratigraphy

Although distinct intervals of reversed and normal polarity are identified in the sedimentary units in Hole U1582A (Cores 1R–5R, 0–31.83 m CSF-A), correlation to the GPTS (Ogg, 2020) is difficult. This is because the sedimentary sequence is considerably condensed and, based on biostratigraphy, ranges from Miocene at the top of Core 1R to Late Cretaceous in Core 4R (see

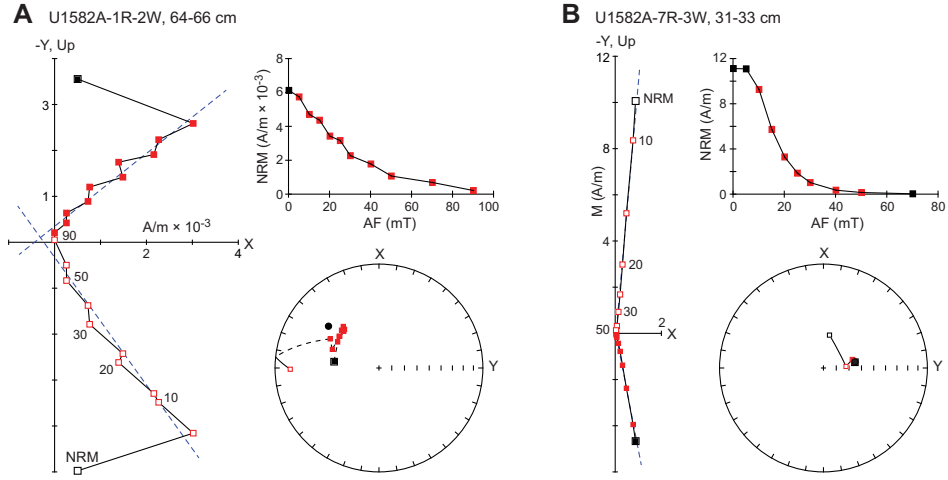

Figure F19. Discrete sample demagnetization results, Hole U1582A. A. Representative vector endpoint diagram (left panel), equal area projection (round panel), and a graph showing natural magnetization (M) decay during demagnetization (top right) from sedimentary Lithostratigraphic Unit I. B. Representative vector endpoint diagram (left panel), equal area projection (round panel), and a graph showing natural magnetization (M) decay during demagnetization (top right) from igneous rocks (Lithostratigraphic Unit II). White symbols = projections onto the vertical plane, black symbols = projections onto the horizontal plane, X and Y = axes of the working halves, and Up = vertical up-pointing (–Z-)axis of the core. Equal-area projections: open symbols = negative (up-pointing) directions, black symbols = positive (down-pointing) directions. All plots: red symbols = steps used to determine the characteristic remanent directions.

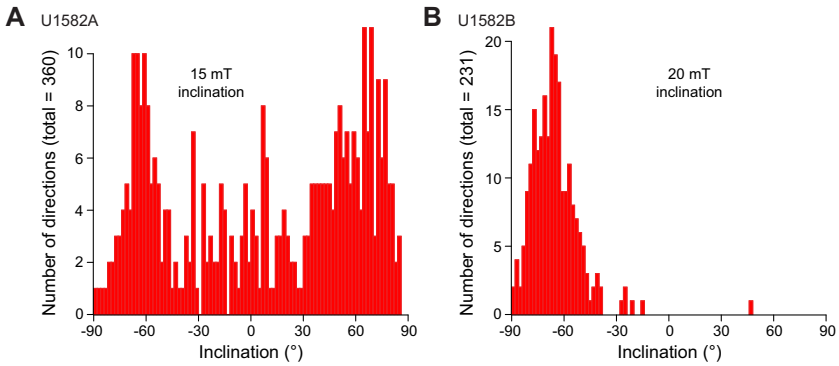

Figure F20. Histogram of all archive-half magnetic inclination data from Holes (A) U1582A and (B) U1582B.

Micropaleontology). All measured basalt in Lithostratigraphic Unit II has normal polarity (Cores 6R and 7R [40.92–48.68 m CSF-A] and 392-U1582B-2R through 5R [36.83–53.73 m CSF-A]). Biostratigraphic data indicate that sediments intercalated with basalt (Hole U1582A = 40.92–48.68 m CSF-A; Hole U1582B = 36.83–53.73 m CSF-A) contain sparse, moderately preserved Late Cretaceous nannofossils of Santonian to Turonian age. This age assignment requires that the normal polarity interval observed in Lithostratigraphic Unit II is in Chron C34n, but this may be modified with additional postcruise biostratigraphic analysis.

7. Chronostratigraphy

Calcareous nannofossils, foraminifera, and magnetostratigraphy provide age control for the Campanian(?) to upper Miocene sediment cores recovered at Site U1582 (see **Micropaleontology** and **Paleomagnetism**). Nannofossils and magnetostratigraphy provide age constraints for the basalt and intercalated sediment of Lithostratigraphic Unit II (see **Lithostratigraphy**). Nannofossils and foraminifera (Table **T4**) combined with magnetostratigraphy provide broad age constraints for the transition between Lithostratigraphic Unit II and Lithostratigraphic Subunit Ib and the sediment above (Lithostratigraphic Unit I). The sedimentary section is very thin (~40 m) at Site U1582, yet it represents a long period of time (as much as 70 My), indicating very low sedimentation rates and/or significant gaps as a result of nondeposition or erosion. The presence of abundant manganese nodules is consistent with this observation. The low sedimentation rates and other processes such as reworking of older sediment and burrowing, together with coring disturbance, make this a particularly challenging site for chronostratigraphy. Because of significant mixing, we infer ages using the youngest age diagnostic taxa in a given sample or set of samples, excluding outliers that appear to result from drilling disturbance or contamination. Below, we describe ages of the sedimentary succession in stratigraphic order from oldest to youngest (Figure **F21**).

7.1. Intercalated basalt and sediment

Sediments intercalated with basalt in Lithostratigraphic Unit II (Hole U1582A = 48.68–40.92 m CSF-A; Hole U1582B = 53.73–36.83 m CSF-A) contain sparse, moderately preserved Late Cretaceous nannofossils. Age diagnostic taxa consistently present in the samples include *E. floralis* (biohorizon top = 84.0 Ma; latest Santonian, n21 in Figure **F21** and Table **T4**) and *E. moratus* (biohorizon base = 93.73 Ma; earliest Turonian; n23, same figure). Taken together, this assemblage suggests an early Turonian to Santonian age (~93.7–84 Ma) for Lithostratigraphic Unit II (Figure **F21**). A few specimens of *E. eximius* s.l. (biohorizon base = 90.36 Ma; mid-Turonian; n22, same figure) in samples from Core 392-U1582A-6R may restrict the age to mid-Turonian or younger, and single specimens of probable *R. anthophorus* (biohorizon base = 86.57 Ma; n20, same figure) in two additional samples may further constrain the age to Coniacian or younger (hatched box in Figure **F21**). However, we place less weight on these very rare occurrences because of difficulties with contamination encountered in samples from this site. The broad age interpretation of Turonian–Santonian is consistent with the persistent normal magnetic polarity of the basalt, which can

therefore be assigned to Superchron C34n. Given the sparse nature of the assemblages, postcruise research may provide additional nannofossil age constraints.

7.2. Sediment

The limestone of Lithostratigraphic Subunit Ib (Hole U1582A = 40.92–31.07 m CSF-A; Hole U1582B = 36.83–36.30 m CSF-A) contains only very rare and poorly preserved Cretaceous nannofossils that provide no additional age control. The limestone shows normal magnetic polarity and no reversals between it and the basalt below. This may suggest that the limestone was deposited during the long Cretaceous Normal Superchron (C34n), indicating an age of Santonian or older; however, this is very tentative.

The nannofossil ooze, clayey silt, sand, and manganese nodules of Lithostratigraphic Subunit Ia (Hole U1582A = 21.76–0 m CSF-A) show predominantly reversed magnetic polarity with some intervals of normal polarity usually associated with manganese nodules (see **Paleomagnetism**). Nannofossil assemblages often include a significant component of reworking and presence of multiple biostratigraphic marker taxa indicating broad age ranges. We identify approximate ages for samples based on the youngest ages in the assemblage and disregard likely contamination from fall-in. Samples 4R-CC, 19–24 cm, to 3R-1, 30 cm (21.71–11.90 m CSF-A), contain a solely Creta-

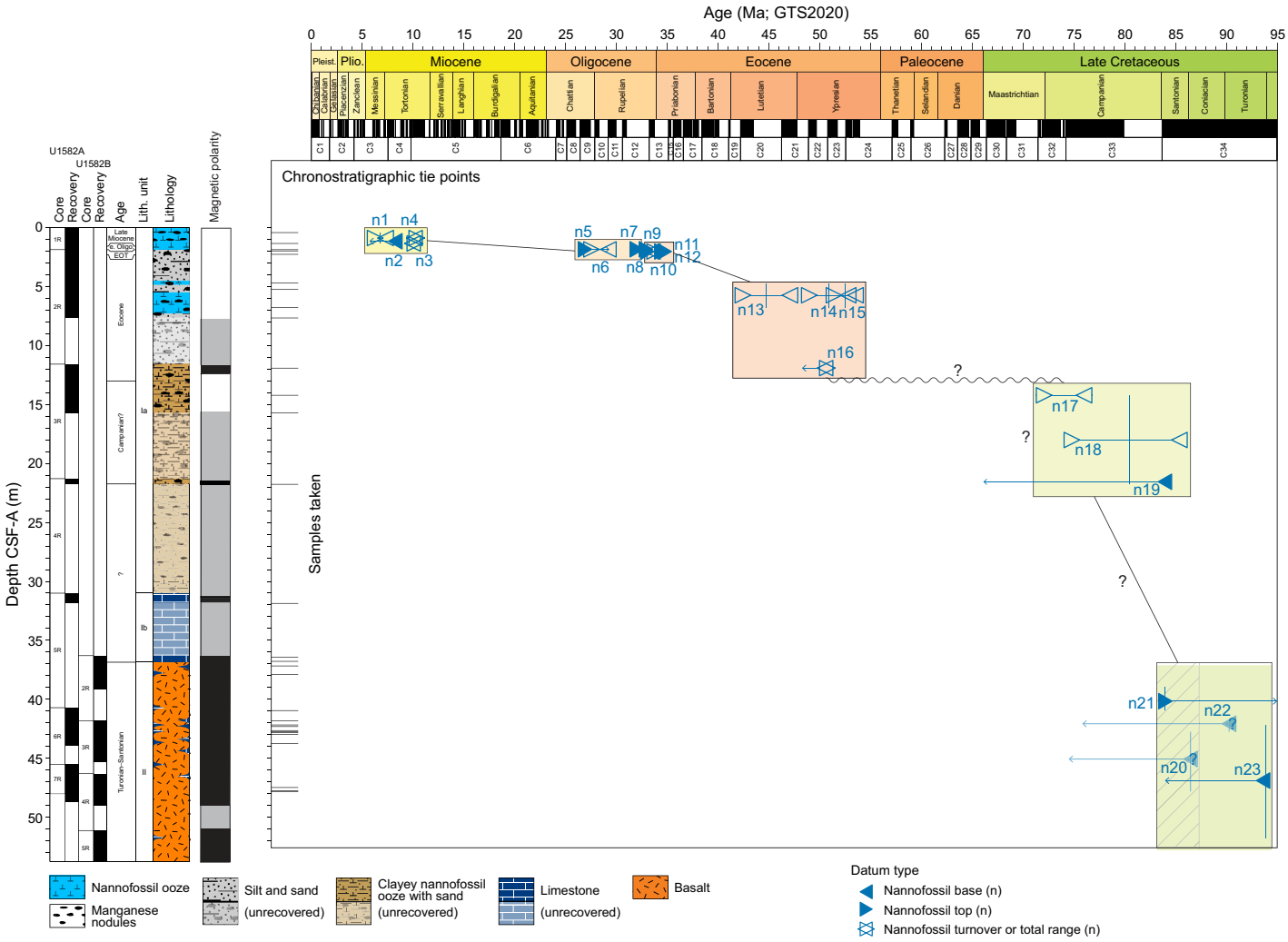

Figure F21. Age-depth model primarily based on calcareous nannofossil biostratigraphy and magnetostratigraphy, Site U1582. Numbers for bioevents correspond to those in Table T4. GTS2020 = Geologic Time Scale 2020 (Gradstein et al., 2020). Colored boxes = approximate ages of sediment packages based on inferred in situ nannofossil assemblages; background color correlates to the geologic timescale. Events n21 and n22 are tentative because they are based on single specimens in only a few samples. Black undulating line = unconformity.

ceous assemblage with background taxa similar to those in the sediment intercalated with the basalt of Lithostratigraphic Unit II. The presence of *A. cymbiformis* (biohorizon base = 83.96 Ma; n19 in Figure **F21** and Table **T4**), *R. anthophorus* (total range = 86.57–74.47 Ma; n20 and n18, same figure), and *U. trifidus* (total range = 76.77–71.31 Ma; n17, same figure) indicates a Campanian to earliest Maastrichtian age (Figure **F21**), despite the dominance of older (Coniacian) species. The predominantly reversed polarity in Core 3R also precludes a Coniacian age. However, we cannot exclude that the nannofossil assemblage is entirely reworked through this interval, which consists of clayey nannofossil ooze with sand and may contain redeposited material (see **Lithostratigraphy**).

Samples 392-U1582A-3R-1, 30 cm (11.90 m CSF-A), and 2R-CC, 5–10 cm (7.63 m CSF-A), contain assemblages of mixed ages with a significant component of older material reworked into younger sediment, together with likely contamination from younger material due to fall-in in the uppermost part of Core 3R. The nannofossil assemblage consists of a mix of Cretaceous taxa similar to those in the deeper samples, as well as Paleogene taxa present in shallower samples. The presence of *Reticulofenestra* spp. indicates an early Eocene or younger age (n16 in Figure **F21** and Table **T4**).

Samples 392-U1582A-2R-4, 35 cm, to 2R-2, 131 cm (6.76–4.71 m CSF-A), contain an early to early middle Eocene nannofossil assemblage that includes *T. orthostylus* (total range = 54.30–50.65 Ma; n15, same figure), *D. lodoensis* (total range = 53.58–48.22 Ma; n14, same figure), and *N. cristata* (total range = 47.85–41.69 Ma; n13, same figure). Preservation is generally poor in these samples, with many coccoliths consisting of only the outer rim; however, some specimens are moderately preserved and allow identification to species level. The deepest sample in this interval also contains a late Paleocene component that is considered reworked.

Sample 392-U1582A-2R-1, 8 cm (1.98 m CSF-A), contains a predominantly Paleogene assemblage with a few specimens of Neogene taxa that we suspect are the result of fall-in at the top of Core 2R (see **Lithostratigraphy**). The sample contains common *C. subdistichus* (n10, same figure), which has an acme between 33.88 and 33.47 Ma immediately following the Eocene/Oligocene boundary, as well as other species with range tops around this interval, including *D. barbadiensis* (biohorizon top = 34.77 Ma; n12, same figure), *D. saipanensis* (biohorizon top = 34.44 Ma; n11, same figure), and *I. recurvus* (biohorizon top = 33.06 Ma; n9, same figure). We assign an age of latest Eocene to earliest Oligocene (~35–33 Ma) to this sample (Figure **F21**). Sample 1R-CC, 14–19 cm (1.85 m CSF-A), contains a slightly younger Oligocene nannofossil assemblage with little or no reworking. We assign a broad age of early to mid-Oligocene (~33 to 27 Ma) based on the presence of *C. formosus* (biohorizon top = 32.92 Ma; n8, same figure), *R. umbilicus* >14 µm (biohorizon top = 32.02 Ma; n7, same figure), *F. distentus* (total range = 30.00–26.81 Ma; n5, same figure), and *F. predistentus* (biohorizon top = 26.93 Ma; n6, same figure).

Samples 392-U1582A-1R-2, 36 cm (1.35 m CSF-A), and 1R-1, 43 cm (0.43 m CSF-A), contain a distinctly different assemblage consisting of predominantly Neogene taxa and only minor numbers of older Paleogene species. Age diagnostic nannofossils include *C. coalitus* (total range = 10.89–9.67 Ma; n4, same figure), *D. hamatus* (total range = 10.57–9.61 Ma; n3, same figure), *D. berggrenii* (biohorizon base = 8.29 Ma; n2, same figure), and *D. quinqueramus* (total range = 8.13–5.53 Ma; n1, same figure) and indicate a late Miocene age between ~10.9 and 5.5 Ma (Figure **F21**). Foraminifera in the mudline sample (0 m CSF-A) indicate a very young (Pleistocene–recent) age for the seafloor sediments.

8. Geochemistry

The geochemistry program at Site U1582 was designed to characterize the composition of bulk sediment and interstitial water (IW) and report on the presence and abundance of volatile hydrocarbons for routine safety monitoring.

8.1. Headspace hydrocarbon gases

In total, six headspace samples were taken and analyzed for routine safety monitoring. All headspace data are reported in Table **T8**, which includes one sample run in duplicate. The samples were typically taken from the top of the deepest section above the core catcher in each core with the exception of lithified cores, where sediment was taken from the section breaks of the core for convenience. Hydrocarbons in headspace samples were detected in Hole U1582A. Methane was above the detection limit in three samples, with concentrations of 0.7 and 0.5 ppmv in Samples 392-U1582A-2R-4, 0–5 cm (6.41 m CSF-A), and 3R-3, 0–5 cm (14.60 m CSF-A). Hydrocarbons with longer chain lengths up to n-hexane (C_6) were not detected in any of the headspace samples.

8.2. Interstitial water geochemistry

Samples for IW were collected from the upper 15 m CSF-A in Hole U1582A, where soft sediment was present (Table **T9**). One IW sample was collected in each of Cores 1R and 3R, and two samples were collected from Core 2R. Alkalinity ranges 2.4–2.9 mM. pH ranges 7.6–7.7. No further shipboard analyses were completed on IW samples from Site U1582 because of the small number of samples collected.

8.3. Bulk sediment geochemistry

In total, five sediment samples were obtained for bulk carbon, nitrogen, and sulfur analyses at Site U1582. One sample was taken from Cores 392-U1582A-1R through 4R, with the exception of two samples taken from Core 2R.

Total carbon and carbonate (where carbonate is reported as calcium carbonate) range 0.2–3.4 wt% and 1.9–28.1 wt% at Site U1582, respectively (see **Lithostratigraphy**) (Table **T10**). Carbonate is elevated (28.1 wt% as $CaCO_3$) in the uppermost sample (392-U1582A-1R-1, 82–83 cm; 0.82 m CSF-A) from Lithostratigraphic Subunit Ia, which is a clayey nannofossil ooze that encompasses the upper 21.76 m CSF-A at this site, as compared to Lithostratigraphic Subunit Ib below 31.07 m CSF-A, which averages 5.2 wt% $CaCO_3$. In Lithostratigraphic Subunit Ib, inorganic carbon averages 0.6 wt%. As a note of caution for the interpretation of these inorganic carbon records, we emphasize that the main carbonate mineral phase may include other carbonate minerals including siderite, dolomite, and possibly others (see **Lithostratigraphy**).

Organic carbon contents are calculated as the difference between the total carbon (elemental analyzer measurement) and inorganic carbon (coulometer measurement), which is generally the difference between two large numbers, thereby making this value imprecise. All organic carbon values are reported in Table **T10**. Values calculated below 0 were set to 0. Total organic carbon is 0 for all samples except Sample 392-U1582A-1R-1, 82–83 cm, which has a concentration of <0.1 wt%.

Total nitrogen was measured but remains low, at or close to the detection limit, for the samples analyzed from Site U1582A. Concentrations remain below 0.1 wt%.

Total sulfur concentrations range from below detection limit to 0.4 wt% (Table **T10**).

Table T8. Gas geochemistry, Site U1582. **Download table in CSV format.**

Table T9. IW data, Site U1582. **Download table in CSV format.**

Table T10. Bulk geochemistry data, Site U1582. **Download table in CSV format.**

9. Physical properties

Standard physical properties measurements were made on Hole U1582A and U1582B cores using the Whole-Round Multisensor Logger (WRMSL), Section Half Multisensor Logger (SHMSL), and Natural Gamma Radiation Logger (NGRL). Discrete measurements were also made for moisture and density (MAD) analysis, thermal conductivity, and *P*-wave velocities using the *P*-wave caliper (PWC) system. The physical properties data from Site U1582 show a progression with depth that delineates the poorly consolidated clayey nannofossil ooze of Lithostratigraphic Subunit Ia (0–21.76 m CSF-A) from the underlying lithified limestone and manganese nodules of Lithostratigraphic Subunit Ib (Hole U1582A = 31.00–40.92 m CSF-A) and from the deeper pillow basalts with interspersed pockets of limestone of Lithostratigraphic Unit II (Hole U1582B = 36.83–53.73 m CSF-A). Lithostratigraphic Subunit Ia contains unlithified sediment with high porosity (65%–82%), low MAD bulk density (1.40–1.62 g/cm^3), low PWC *P*-wave velocities (~1600 m/s), and low thermal conductivity (0.9–1.2 W/[m·K]). In comparison, the underlying more lithified limestones of Lithostratigraphic Subunit Ib have much lower porosity (~25%), higher average PWC *P*-wave velocity (~3000 m/s), and higher bulk density (~2.33 g/cm^3). The dark-colored pillow basalts (L* = ~20 to 40, lightness) of Lithostratigraphic Unit II have higher NGR (~20 counts/s) and MS (~500–1000 instrument units [IU] using the WRMSL) than the light-colored basalts, which likely reflects a higher degree of alteration.

9.1. Natural gamma radiation

NGR at Site U1582 generally ranges 5–25 counts/s (Figure **F22**). These values are lower than the clay-rich lithologies at Site U1581 in the Transkei Basin and are more similar to the carbonate-rich and igneous lithologies at Sites U1579 and U1580 on the Agulhas Plateau. NGR generally decreases with depth from 10–25 counts/s in the clayey nannofossil oozes of Lithostratigraphic Subunit Ia (0–30.00 m CSF-A) to 5–25 counts/s in the pillow basalts and interspersed limestones of Lithostratigraphic Unit II (36.83–53.73 m CSF-A). A spike in NGR to ~45 counts/s that occurs in the upper part of Core 392-U1582A-2R is likely due to the presence of fall-in material given the observed drilling disturbance and presence of manganese nodules (see **Lithostratigraphy**).

Deconvolution of NGR energy spectra from the NGRL indicates that both K and U are elevated at the top of the basalt layer (Lithostratigraphic Unit II) at ~36–38 m CSF-A where limonite and dendritic manganese and calcite veins are found at the contact with the basalt (see

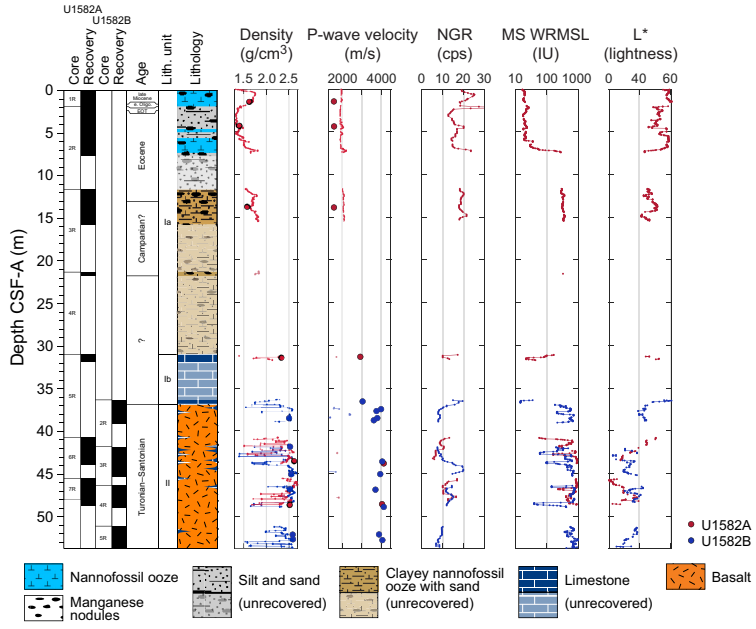

Figure F22. Physical properties, Holes U1582A and U1582B. cps = counts per second.

Lithostratigraphy). Below this depth interval, K is the primary driver of fluctuations in the total NGR signal. Because K is typically abundant in specific clay minerals and K contents are elevated as high as 3 wt% in several igneous units, the NGR signal in Lithostratigraphic Unit II appears to reflect the abundant presence of clay mineral alteration products (Figure **F23**). The decreasing trend in NGR below ~45 m CSF-A may therefore indicate a decrease of basalt alteration toward the base of Hole U1582B (Figure **F12**).

9.2. Color reflectance

Color properties of section halves were measured using the SHMSL and Section Half Imaging Logger (SHIL). The range of L* decreases with depth from ~40 to 60 in the lighter clayey nannofossil ooze of Lithostratigraphic Unit I (0–36.83 m CSF-A) to 20–60 in the darker pillow basalts with interspersed limestones of Lithostratigraphic Unit II (36.83–53.73 m CSF-A) (Figure **F22**). Similarly, the green versus red contrast as measured by the parameter a* shifts to lower values with depth at Site U1582. The clayey nannofossil oozes of Lithostratigraphic Subunit Ia (0–31.00 m CSF-A) have higher a* values (~5–10), whereas a* values in the pillow basalts and interspersed limestones of Lithostratigraphic Unit II are –5 to 6 (see Figure **F12**).

9.3. Magnetic susceptibility

MS values measured on the WRMSL and SHMSL range across two orders of magnitude between the different lithostratigraphic units at Site U1582 (Figure **F22**). MS differentiates lithologies, showing low to moderate values (~10–400 IU) for sediments and high values (>~400 IU) for igneous lithologies. Notably, an order of magnitude increase in MS occurs below ~7 m CSF-A in the clayey nannofossil ooze of Lithostratigraphic Subunit Ia, although the source of this jump is unclear. There is high variability in MS in Lithostratigraphic Unit II (36.83–53.73 m CSF-A) because of the interbedding of pillow basalts and limestones.

9.4. Bulk density, grain density, and porosity

The bulk density of whole-round sections from Site U1582 was measured by gamma ray attenuation (GRA) bulk density using the WRMSL. Additionally, MAD measurements were made for 12 discrete samples at a resolution of 2 samples per full core or 1 sample per half core (Figure **F24**). Because of the incomplete filling of the core liner with the RCB cores, GRA bulk density is less accurate and on average 0.2–0.3 g/cm^3 lower than MAD bulk density. After applying a volume

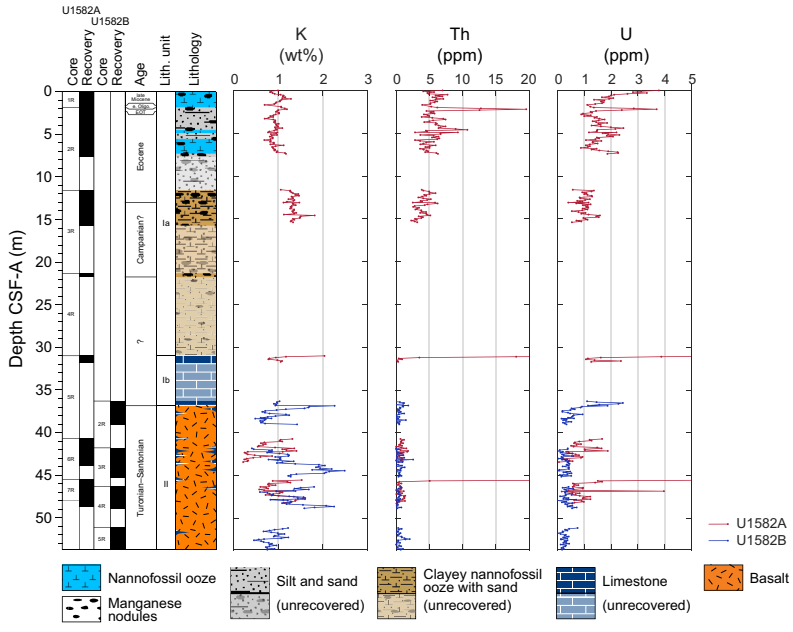

Figure F23. Deconvolved NGR data, Hole U1582B.

correction to raw GRA bulk density data (see **Physical properties** in the Expedition 392 methods chapter [Uenzelmann-Neben et al., 2023a]), density values obtained using these two methods are similar (Figure **F22**). The average MAD bulk density of sediments of Lithostratigraphic Subunit Ia ranges 1.4–1.6 g/cm^3 (0–31.00 m CSF-A). MAD bulk density increases in the limestone of Lithostratigraphic Subunit Ib (31.00–36.83 m CSF-A) to ~2.3 g/cm^3 (Figure **F24**). Bulk density ranges 2.5–2.6 g/cm^3 in the underlying basalts of Lithostratigraphic Subunit II (36.83–53.73 m CSF-A).

The MAD porosity of lithologies at Site U1582 is very high (~60%–85%) in the clayey nannofossil ooze of Lithostratigraphic Subunit Ia (0–31.00 m CSF-A) (Figure **F24**). MAD porosity decreases to 25% in the limestones of Lithostratigraphic Subunit Ib (31.00–36.83 m CSF-A) and ~16%–20% in the basalts of Lithostratigraphic Unit II (36.83–53.73 m CSF-A). Although this decrease with depth is substantial, the average MAD porosity of the basalts at Site U1582 is higher than that of the basalts at Sites U1579 and U1580, which is consistent with more intense alteration at Site U1582 (see **Igneous petrology**). The high MAD grain density of ~2.8–3.2 g/cm^3 for the sediments of Lithostratigraphic Unit I (0–36.83 m CSF-A) may relate to the abundance of manganese oxides at the site (Figure **F24**). Given the poor correlation between MAD bulk density and MAD grain density, it appears that reduction in porosity is the main driver of increasing bulk density with depth at Site U1582 (Figure **F25C, F25D**).

9.5. *P*-wave velocity

The *P*-wave velocities of cores from Site U1582 were measured using the *P*-wave logger (PWL) on the WRMSL at a spatial resolution of 2.5 cm and the PWC for one to two measurements per core in Hole U1582A and one measurement per section in Hole U1582B. Section halves of igneous rocks were immersed in a seawater bath under vacuum for 6 h of soaking prior to measurement on the PWC (see **Physical properties** in the Expedition 392 methods chapter [Uenzelmann-Neben et al., 2023a]). PWL measurements on whole-round sections in Hole U1582B did not provide reliable results due to large voids in the core liners (Figure **F22**). PWC velocities increase with depth and positively correlate with MAD bulk density and thermal conductivity. PWC velocity averages ~1590 m/s in the clayey nannofossil ooze of Lithostratigraphic Subunit Ia (0–31.00 m CSF-A) and increases to an average of ~3000 m/s in the limestone of Lithostratigraphic Subunit Ib (31.00–36.83 m CSF-A) (Figure **F22**). The average PWC velocity increases substantially to 3900–4100 m/s in the pillow basalts and interspersed limestones of Lithostratigraphic Unit II (36.83–53.73 m CSF-A).

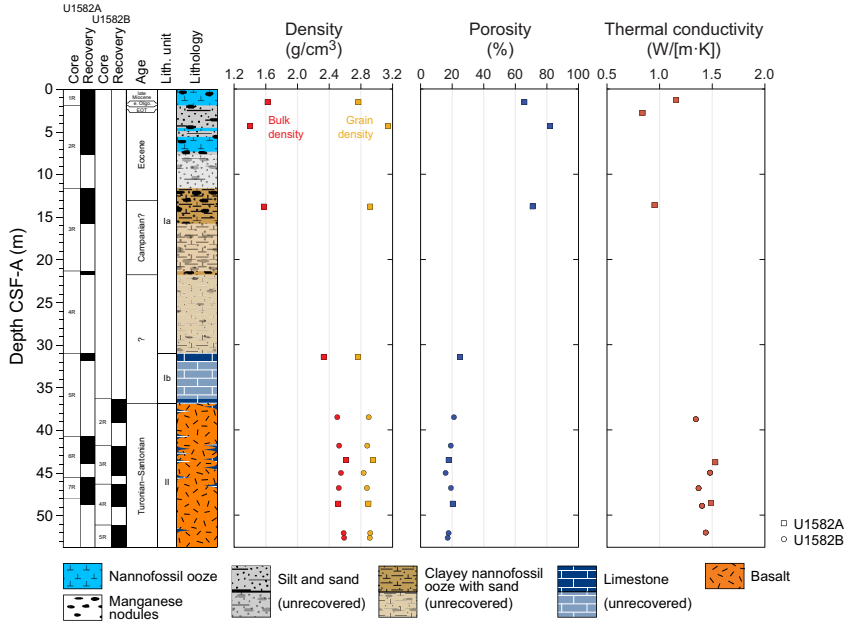

Figure F24. MAD and thermal conductivity results, Site U1582.

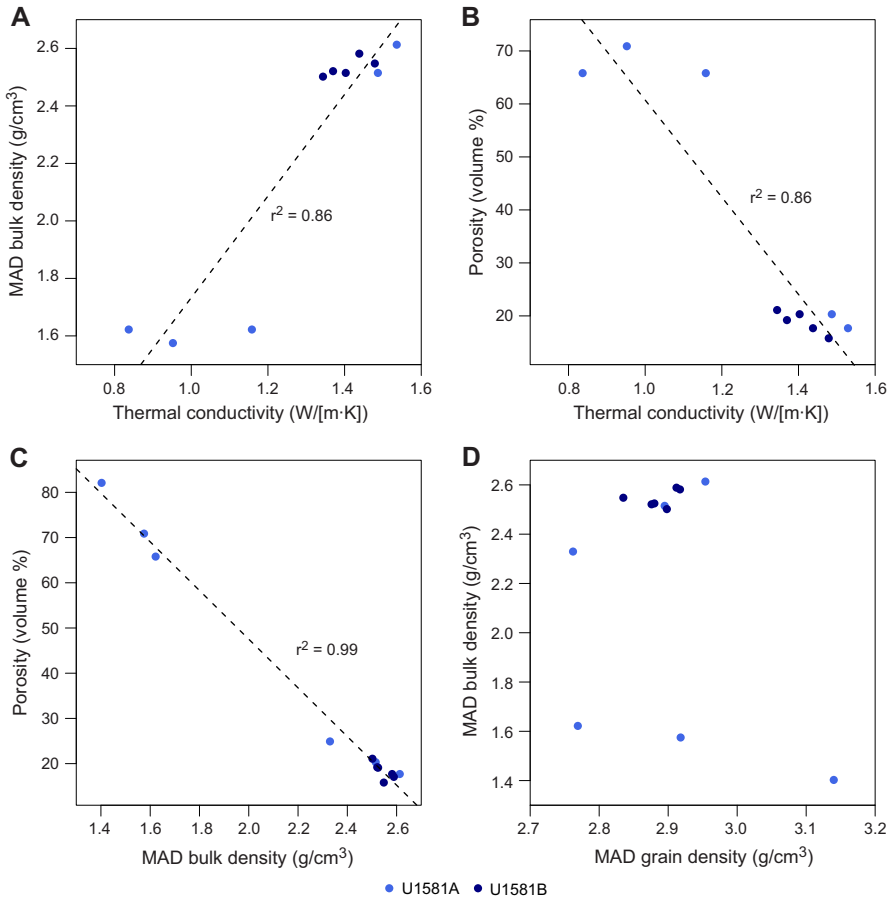

Figure F25. MAD results, Site U1582. A. MAD bulk density vs. thermal conductivity. B. MAD porosity vs. thermal conductivity. C. MAD porosity vs. MAD bulk density. D. MAD bulk density vs. MAD grain density. For cross-plotting, thermal conductivity data were paired with the closest MAD measurement with a maximum depth offset of 1.24 m between observations.

9.6. Thermal conductivity

Thermal conductivity was measured on section halves using a puck probe. Section halves of igneous rocks were immersed in seawater during measurement following 6 h of soaking in a seawater bath under vacuum (see **Physical properties** in the Expedition 392 methods chapter [Uenzelmann-Neben et al., 2023a]). Thermal conductivity at Site U1582 correlates inversely with porosity and positively with MAD bulk density (Figure **F25A, F25B**). Thermal conductivity increases substantially from 0.87–1.16 W/(m·K) in the clayey nannofossil ooze of Lithostratigraphic Subunit I (0–36.83 m CSF-A) to 1.37–1.53 W/(m·K) in the pillow basalts and interspersed limestones of Lithostratigraphic Unit II (36.83–53.73 m CSF-A) (Figure **F24**). These values are generally ~0.2–0.3 W/(m·K) lower than for igneous units at Sites U1579 and U1580, which may indicate more porosity and/or alteration of the pillow basalts at Site U1582.

References

Backman, J., 1987. Quantitative calcareous nannofossil biochronology of middle Eocene through early Oligocene sediment from DSDP Sites 522 and 523. Abh. Geology, 39:21–31. **https://web.archive.org/web/20190430234835id_/https://www.zobodat.at/pdf/AbhGeolBA_39_0021-0032.pdf**

Batiza, R., and White, J.D.L., 2000. Submarine lavas and hyaloclastite. In Sigurdsson, H., Encyclopedia of Volcanoes. San Diego, CA (Academic Press), 361–381.

Bohaty, S.M., Uenzelmann-Neben, G., Childress, L.B., Archontikis, O.A., Batenburg, S.J., Bijl, P.K., Burkett, A.M., Cawthra, H.C., Chanda, P., Coenen, J.J., Dallanave, E., Davidson, P.C., Doiron, K.E., Geldmacher, J., Gürer, D., Haynes, S.J., Herrle, J.O., Ichiyama, Y., Jana, D., Jones, M.M., Kato, C., Kulhanek, D.K., Li, J., Liu, J., McManus, J.,

Minakov, A.N., Penman, D.E., Sprain, C.J., Tessin, A.C., Wagner, T., and Westerhold, T., 2023. Site U1580. In Uenzelmann-Neben, G., Bohaty, S.M., Childress, L.B., and the Expedition 392 Scientists, Agulhas Plateau Cretaceous Climate. Proceedings of the International Ocean Discovery Program, 392: College Station, TX (International Ocean Discovery Program). **https://doi.org/10.14379/iodp.proc.392.104.2023**

Coffin, M.F., and Eldholm, O., 2001. Large igneous provinces: progenitors of some ophiolites? In Ernst, R.E. and Buchan, K.L. (Eds.), Mantle Plumes: Their Identification Through Time. Special Paper - Geological Society of America, 352. **https://doi.org/10.1130/0-8137-2352-3.59**

Dunlop, D.J., and Özdemir, Ö., 1997. Rock Magnetism: Fundamentals and Frontiers: Cambridge, United Kingdom (Cambridge University Press). **https://doi.org/10.1017/CBO9780511612794**

Fioroni, C., Villa, G., Persico, D., Wise, S.W., and Pea, L., 2012. Revised middle Eocene-upper Oligocene calcareous nannofossil biozonation for the Southern Ocean. Revue de Micropaléontologie, 55(2):53–70. **https://doi.org/10.1016/j.revmic.2012.03.001**

Gohl, K., and Uenzelmann-Neben, G., 2001. The crustal role of the Agulhas Plateau, southwest Indian Ocean: evidence from seismic profiling. Geophysical Journal International, 144(3):632–646. **https://doi.org/10.1046/j.1365-246x.2001.01368.x**

Gohl, K., Uenzelmann-Neben, G., and Grobys, N., 2011. Growth and dispersal of a Southeastern African Large Igneous Province. South African Journal of Geology, 114(3–4):379–386. **https://doi.org/10.2113/gssajg.114.3-4.379**

Gradstein, F.M., Ogg, J.G., Schmitz, M.D., and Ogg, G.M. (Eds.), 2020. The Geologic Time Scale 2020: Amsterdam (Elsevier BV). **https://doi.org/10.1016/C2020-1-02369-3**

Homrighausen, S., Hoernle, K., Geldmacher, J., Wartho, J.A., Hauff, F., Portnyagin, M., Werner, R., van den Bogaard, P., and Garbe-Schönberg, D., 2018. Unexpected HIMU-type late-stage volcanism on the Walvis Ridge. Earth and Planetary Science Letters, 492:251–263. **https://doi.org/10.1016/j.epsl.2018.03.049**

Jacques, G., Hauff, F., Hoernle, K., Werner, R., Uenzelmann-Neben, G., Garbe-Schönberg, D., and Fischer, M., 2019. Nature and origin of the Mozambique Ridge, SW Indian Ocean. Chemical Geology, 507:9–22. **https://doi.org/10.1016/j.chemgeo.2018.12.027**

Jordan, B., Fowler, A.-R., Mahmoud, B., El-Saiy, A., and Abdelghanny, O., 2008. Peperites and associated pillow lavas subjacent to the Oman Ophiolite. Journal of Volcanology and Geothermal Research, 173:303–312. **https://doi.org/10.1016/j.jvolgeores.2008.01.019**

Kirschvink, J.L., 1980. The least-squares line and plane and the analysis of paleomagnetic data. Geophysical Journal International, 62(3):699–718. **https://doi.org/10.1111/j.1365-246X.1980.tb02601.x**

Lurcock, P.C., and Wilson, G.S., 2012. PuffinPlot: a versatile, user-friendly program for paleomagnetic analysis. Geochemistry, Geophysics, Geosystems, 13(6):Q06Z45. **https://doi.org/10.1029/2012GC004098**

Martini, E., 1971. Standard Tertiary and Quaternary calcareous nannoplankton zonation. Proceedings of the Second Planktonic Conference, Roma, 1970:739–785.

Ogg, J.G., 2020. Geomagnetic Polarity Time Scale. In Gradstein, F.M., Ogg, J.G., Schmitz, M., and Ogg, G. (Eds.), Geologic Time Scale 2020. Amsterdam (Elsevier), 159–192. **https://doi.org/10.1016/B978-0-12-824360-2.00005-X**

Petrizzo, M.R., MacLeod, K.G., Watkins, D.K., Wolfgring, E., and Huber, B.T., 2022. Late Cretaceous paleoceanographic evolution and the onset of cooling in the Santonian at southern high latitudes (IODP Site U1513, SE Indian Ocean). Paleoceanography and Paleoclimatology, 37(1):e2021PA004353. **https://doi.org/10.1029/2021PA004353**

Sissingh, W., 1977. Biostratigraphy of Cretaceous calcareous nannoplankton. Geologie en Mijnbouw, 56:37–65.

Skilling, I.P., White, J.D.L., and McPhie, J., 2002. Peperite: a review of magma–sediment mingling. Journal of Volcanology and Geothermal Research, 114(1–2):1–17. **https://doi.org/10.1016/S0377-0273(01)00278-5**

Uenzelmann-Neben, G., Bohaty, S.M., Childress, L.B., Archontikis, O.A., Batenburg, S.J., Bijl, P.K., Burkett, A.M., Cawthra, H.C., Chanda, P., Coenen, J.J., Dallanave, E., Davidson, P.C., Doiron, K.E., Geldmacher, J., Gürer, D., Haynes, S.J., Herrle, J.O., Ichiyama, Y., Jana, D., Jones, M.M., Kato, C., Kulhanek, D.K., Li, J., Liu, J., McManus, J., Minakov, A.N., Penman, D.E., Sprain, C.J., Tessin, A.C., Wagner, T., and Westerhold, T., 2023a. Expedition 392 methods. In Uenzelmann-Neben, G., Bohaty, S.M., Childress, L.B., and the Expedition 392 Scientists, Agulhas Plateau Cretaceous Climate. Proceedings of the International Ocean Discovery Program, 392: College Station, TX (International Ocean Discovery Program). **https://doi.org/10.14379/iodp.proc.392.102.2023**

Uenzelmann-Neben, G., Bohaty, S.M., Childress, L.B., Archontikis, O.A., Batenburg, S.J., Bijl, P.K., Burkett, A.M., Cawthra, H.C., Chanda, P., Coenen, J.J., Dallanave, E., Davidson, P.C., Doiron, K.E., Geldmacher, J., Gürer, D., Haynes, S.J., Herrle, J.O., Ichiyama, Y., Jana, D., Jones, M.M., Kato, C., Kulhanek, D.K., Li, J., Liu, J., McManus, J., Minakov, A.N., Penman, D.E., Sprain, C.J., Tessin, A.C., Wagner, T., and Westerhold, T., 2023b. Expedition 392 summary. In Uenzelmann-Neben, G., Bohaty, S.M., Childress, L.B., and the Expedition 392 Scientists, Agulhas Plateau Cretaceous Climate. Proceedings of the International Ocean Discovery Program, 392: College Station, TX (International Ocean Discovery Program). **https://doi.org/10.14379/iodp.proc.392.101.2023**